Journal of Energy Chemistry 81 (2023) 574–582

Contents lists available at ScienceDirect

Journal of Energy Chemistry

journal homepage: www.elsevier.com/locate/jechem

http://www.journals.elsevier.com/journal-of-energy-chemistry/

Ultralow-voltage hydrogen production and simultaneous Rhodamine B beneficiation in neutral wastewater

Xiang Peng [a,b], Song Xie [a], Shijian Xiong [a], Rong Li [a], Peng Wang [a], Xuming Zhang [c], Zhitian Liu [a,*], Liangsheng Hu [d], Biao Gao [c,*], Peter Kelly [e], Paul K. Chu [b,*]

[a] Hubei Key Laboratory of Plasma Chemistry and Advanced Materials, Hubei Engineering Technology Research Center of Optoelectronic and New Energy Materials, School of Materials Science and Engineering, Wuhan Institute of Technology, Wuhan 430205, Hubei, China
[b] Department of Physics, Department of Materials Science and Engineering, Department of Biomedical Engineering, City University of Hong Kong, Tat Chee Avenue, Kowloon 999077, Hong Kong, China
[c] State Key Laboratory of Refractories and Metallurgy and Institute of Advanced Materials and Nanotechnology, Wuhan University of Science and Technology, Wuhan 430081, Hubei, China
[d] Department of Chemistry and Key Laboratory for Preparation and Application of Ordered Structural Materials of Guangdong Province, Shantou University, Shantou 515063, Guangdong, China
[e] Surface Engineering Group, Manchester Metropolitan University, Manchester M1 5GD, UK

ARTICLE INFO

Article history:
Received 3 February 2023
Revised 8 March 2023
Accepted 11 March 2023
Available online 29 March 2023

Keywords:
Energy-saving hydrogen production
Hydrogen evolution reaction
Neutral water splitting
$MoSe_2/MoO_2$ heterostructure
Environmental recovery

ABSTRACT

Electrocatalytic water splitting for hydrogen production is hampered by the sluggish oxygen evolution reaction (OER) and large power consumption and replacing the OER with thermodynamically favourable reactions can improve the energy conversion efficiency. Since iron corrodes easily and even self-corrodes to form magnetic iron oxide species and generate corrosion currents, a novel strategy to integrate the hydrogen evolution reaction (HER) with waste Fe upgrading reaction (FUR) is proposed and demonstrated for energy-efficient hydrogen production in neutral media. The heterostructured $MoSe_2/MoO_2$ grown on carbon cloth (MSM/CC) shows superior HER performance to that of commercial Pt/C at high current densities. By replacing conventional OER with FUR, the potential required to afford the anodic current density of 10 mA cm^{-2} decreases by 95%. The HER/FUR overall reaction shows an ultralow voltage of 0.68 V for 10 mA cm^{-2} with a power equivalent of 2.69 kWh per m^3 H_2. Additionally, the Fe species formed at the anode extract the Rhodamine B (RhB) pollutant by flocculation and also produce nanosized magnetic powder and beneficiated RhB for value-adding applications. This work demonstrates both energy-saving hydrogen production and pollutant recycling without carbon emission by a single system and reveals a new direction to integrate hydrogen production with environmental recovery to achieve carbon neutrality.

1. Introduction

Electrochemical water splitting driven by sustainable energy is one of the promising techniques to produce high-purity hydrogen in the global efforts to replace fossil fuels and achieve carbon neutrality [1,2]. The efficiency of hydrogen production depends on the physicochemical and electrochemical properties of the electrocatalytic couples and electrocatalysts [3,4]. Electrochemical water splitting consists of hydrogen evolution reaction (HER) on the cathode and oxygen evolution reaction (OER) on the anode. OER is considered the rate-determining step due to the large theoretical potential barrier ($4OH^- \rightarrow O_2 + 2H_2O + 4e^-$, 1.23 V *vs.* RHE) in addition to a big overpotential, thus entailing high electricity consumption [5,6]. Therefore, developing a thermodynamically easier and less energy-demanding reaction to replace OER is critical.

Recently, thermodynamically favourable oxidation of small molecules and organic species have been integrated to produce hydrogen by HER [7–10]. For instance, Qian et al. have utilized hydrazine oxidation to replace OER and the two-electrode electrolyzer requires cell voltages of 0.071 and 0.76 V for 10 and 400 mA cm^{-2}, respectively [11]. The combination of electrooxidation of organic pollutants and HER is a promising solution for the simultaneous treatment of wastewater and renewable energy generation [12]. Sun et al. have demonstrated hydrogen production by

* Corresponding authors.
E-mail addresses: able.ztliu@wit.edu.cn (Z. Liu), gaobiao@wust.edu.cn (B. Gao), paul.chu@cityu.edu.hk (P.K. Chu).

https://doi.org/10.1016/j.jechem.2023.03.022

hybrid seawater splitting coupled with hydrazine degradation, which presents a low electricity equivalent of 2.75 kWh per m^3 H_2, thus enabling hydrogen production and removal of harmful pollutants at the same time [13]. These strategies have been shown to improve the energy efficiency of hydrogen production but the gaseous products either need purification or contribute to carbon emission. Moreover, the kinetics of HER and anodic reaction must match to improve the Faradaic efficiency in the overall reaction.

Transition metal-based electrocatalysts undergo reconstruction before OER, during which metal atoms with a low valence state are oxidized to a higher valence to produce an oxidation current with thermodynamic favorability [14]. Hence, it is possible to replace OER with the metal oxidation reaction and couple it with HER to facilitate hydrogen production. However, this strategy has seldom been reported so far, perhaps because metal oxidation consumes the anode, consequently raising the operating and materials costs. Electrochemical flocculation has been used in environmental fields to remove pollutants including heavy metal ions and organic species, especially Rhodamine B (RhB), which is an industrial pollutant produced universally by the textile, plastics, leather, dyeing, paper, and printing industries and its disposal can cause serious environmental concerns [15,16]. Moreover, beneficiated RhB is produced when releasing flocculated RhB into a solution with a smaller volume and electrochemical flocculation proceeds at a positive potential via the Fe oxidation reaction in neutral media to form the flocculant (hydroxy complex, polynuclear hydroxy complex, and hydroxide) [17]. In addition, Fe tends to self-corrode and form magnetic oxide species (Fe upgrading reaction, FUR), even though applying a very small positive potential can facilitate FUR [18]. Therefore, integrating HER and FUR may result in highly efficient hydrogen production. However, the design and construction of high-performance HER electrocatalysts for neutral water splitting are still challenging.

Despite the excellent HER capability of Pt- and Ru-based noble catalysts [19–21], more cost-effective candidates such as metal carbides [22,23], metal phosphides [24,25], metal sulfides [26,27], metal nitrides [28,29], and metal selenides [30,31] are being explored as replacements. In particular, two-dimensional layered molybdenum selenides ($MoSe_2$) have attracted much attention due to the favourable hydrogen adsorption free energy (ΔG_H) and tunable active sites [32,33]. $MoSe_2$ normally exists in the 1*T* and 2*H* phases. 2*H*-$MoSe_2$ is an indirect bandgap semiconductor with low conductivity, whereas 1*T*-$MoSe_2$ has metallic behaviour and better HER capability albeit poorer stability [34,35]. Qu et al. have prepared the Mo/(1*T*-2*H*)-$MoSe_2$ composite which shows a small Tafel slope of 35 mV dec^{-1} and good stability [36]. Deng et al. have constructed the bi-phase (1*T*-2*H*)-$MoSe_2$ on a conductive substrate and shown a small overpotential of 126 mV to achieve 10 mA cm^{-2} [37]. Their results indicate that the 2*H*-$MoSe_2$ substrate can modify the electronic structure of 1*T*-$MoSe_2$, which serves as the main active center in the (1*T*-2*H*)-$MoSe_2$ electrocatalyst. However, $MoSe_2$ is oxidized quite easily, consequently compromising long-term stability. Nevertheless, combining electrochemically active 1*T*-$MoSe_2$ with highly conductive and stable Mo-based oxides may be a good strategy to produce highly active and stable composite electrocatalysts.

Herein, we propose to realize energy-saving and efficient hydrogen production by a combined water-splitting and pollutant-extracting strategy in neutral wastewater. In the process, electrolysis of neutral water on the cathode produces high-purity hydrogen via HER, while Fe is converted into Fe^{2+} at the anode via FUR instead of OER. HER is catalyzed by the heterostructured $MoSe_2/MoO_2$ composite grown on carbon cloth (MSM/CC) produced by in situ phase separation. Fe^{2+} generated on the anode forms the $Fe(OH)_2$ to adsorb RhB by flocculation to facilitate wastewater purification. Meanwhile, magnetic Fe_3O_4 nanoparticles are produced. All in all, the process produces hydrogen and removes RhB pollutant at the same time without carbon emission, as schematically illustrated in Scheme 1. The HER/FUR couple requires 0.68 V to generate a current density of 10 mA cm^{-2} and can be powered by solar cells with an electricity equivalent of 2.69 kWh per m^3 H_2 in neutral media. The results reveal a new direction to realize energy-efficient hydrogen production in neutral media with zero-carbon emission and environmental recovery.

2. Experimental

2.1. Material preparation

2.1.1. Synthesis of MoO_3/CC

The MoO_3 nanowire arrays were grown on carbon cloth (CC) by a solution method. In detail, 0.9 g of $(NH_4)_2MoO_4$ was added to a solution (50 mL) containing HNO_3 and deionized water (DW) with a volume ratio of 4:1. A piece of clean CC (2 × 3 cm^2) was immersed in the solution and then heated to 70 °C for 1 h in a water bath. The product was designated as MoO_3/CC.

2.1.2. Synthesis of MSM/CC

The $MoSe_2/MoO_2$ core–shell structure was prepared by chemical vapor deposition (CVD). MoO_3/CC and 1.0 g of Se powder were put on two separate porcelain plates with the Se powder upstream in the tube furnace. MoO_3/CC was heated to 400 °C for 1 h at a ramping rate of 5 °C min^{-1} under N_2/H_2 (containing H_2 of 8%) and then cooled to room temperature. The product was designated as MSM/CC.

2.1.3. Synthesis of $MoSe_2$/CC and MoO_2/CC

Pure $MoSe_2$ was prepared by CVD similar to that for MSM/CC except that the temperature was 500 °C. The product was designated as $MoSe_2$/CC. Pure MoO_2 was prepared by hydrogen reduction, in which MoO_3/CC was put in a tube furnace, heated to 550 °C for 3 h under N_2/H_2 (containing H_2 of 8%), and cooled to room temperature. The product was designated as MoO_2/CC.

2.2. Materials characterization

The morphology and composition of the samples were characterized by field-emission scanning electron microscopy (FE-SEM, TESCAN MIRA LMS), transmission electron microscopy (TEM, FEI F200), high-resolution TEM (HR-TEM) equipped with energy dispersive X-ray (EDX) spectroscopy, X-ray diffraction (XRD, LabX XRD-6100, Shimadzu) with a Cu K_α source, and Raman scattering (HR RamLab). X-ray photoelectron spectroscopy (XPS, Thermo Scientific K-Alpha, Thermo Fisher) was performed with monochromatic Al K_α X-ray to determine the chemical state of the samples and the binding energy of 284.8 eV of C 1*s* was the reference. The conductivity was evaluated by a four-point probe using the Keithley 2450. The magnetic properties were investigated on the vibrating sample magnetometer (Lakeshore 7404). The total organic carbon (TOC) in the electrolyte was measured by a carbon analyzer (Elementar Vario TOC). The UV–visible (UV-vis) spectra were acquired on the PerkinElmer Lambda 35 and Fourier transform infrared (FT-IR) spectra were obtained on the PerkinElmer Spectrum Two.

2.3. Electrochemical measurements

The electrochemical measurements were carried out based on the three-electrode configuration on the CHI 760E (Shanghai CH Instrument, China). The reference and counter electrodes were the saturated calomel electrode (SCE) and graphite rod,

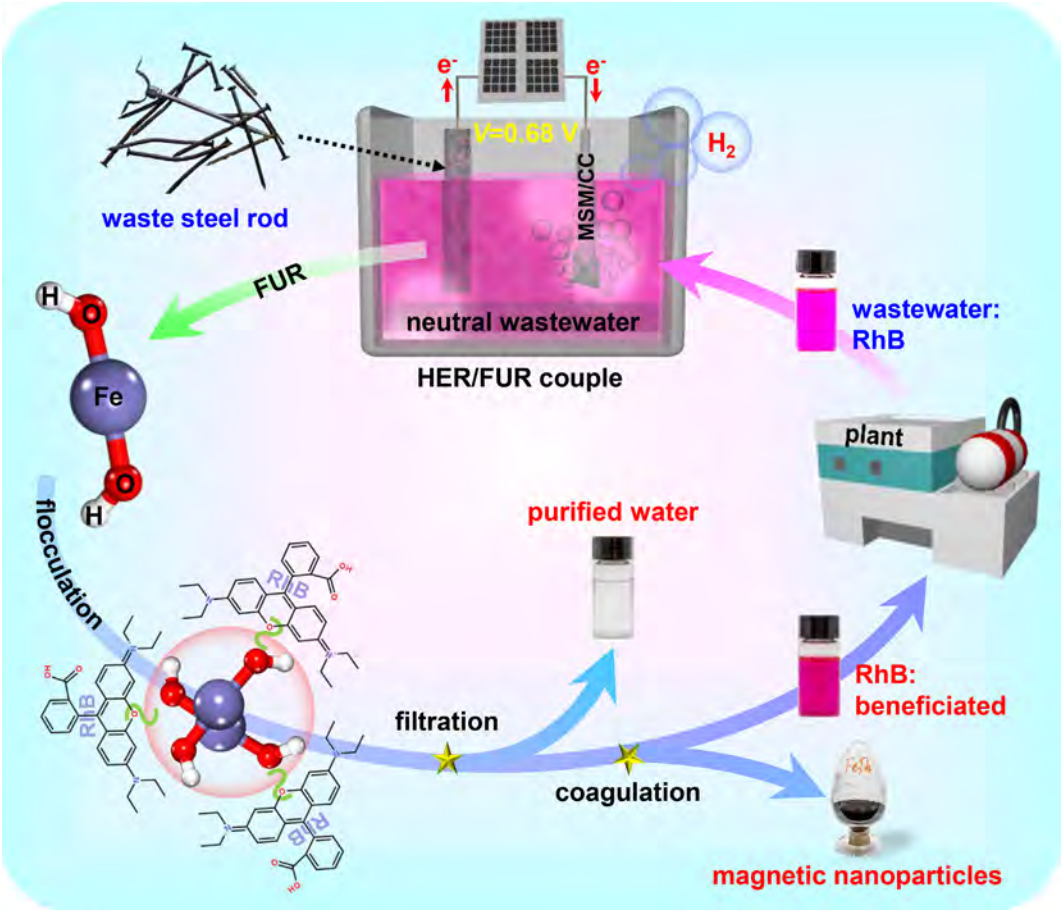

Scheme 1. Schematically illustration of the concept of HER/FUR couple for ultralow-voltage hydrogen production and simultaneous magnetic Fe_3O_4 nanoparticles production, wastewater purification as well as RhB beneficiation in neutral media.

respectively. The CC modified with the nanostructure serves as the working electrode (cathode) in HER (overall reaction). A typical waste steel rod used for construction was used as the working electrode (anode) in FUR (overall reaction). All the potentials in HER were *iR* corrected and calibrated to the reversible hydrogen electrode (RHE) by the Nernst equation $E(\text{RHE}) = E(\text{SCE}) + 0.242 + 0.059 \times \text{pH}$, where the pH values of 0.5 M H_2SO_4, 1.0 M KOH, and 0.5 M Na_2SO_4 were 0.48, 13.58, and 5.80 (FE28, Mettler Toledo), respectively. Linear sweep voltammetry (LSV) was conducted at a scanning rate of 5 mV s^{-1} and the Tafel slope was calculated from the linear portion of the Tafel plot. Electrochemical impedance spectroscopy (EIS) was performed with an amplitude of 5 mV in the frequency range of 100 kHz ~ 0.1 Hz. The electrochemically active surface area (ECSA) was determined by cyclic voltammetry (CV) in the potential range between –0.5 and –0.6 V *vs.* SCE. The HER stability was determined at a potential of –1.4 V *vs.* SCE and the amount of H_2 produced was measured by the water displacement method.

3. Results and discussion

3.1. Structure of the catalysts

Fig. S1 illustrates the preparation of the core–shell $MoSe_2/MoO_2$ composite. The MoO_3 nanowires are grown on CC (MoO_3/CC) by a solution method and then phase-separated to form the core–shell $MoSe_2/MoO_2$ on CC (MSM/CC). The surface morphological evolution during phase separation is schematically presented in Fig. 1 (a) and confirmed by morphological characterization. FE-SEM images in Fig. S2(a and b) show that the uniform nanowire array with a smooth surface covers the carbon fibers. After CVD for selenation, the nanowire array structure remains, but the surface becomes rough and sheet-like (Fig. 1b and c). In addition, the diameter of the nanowire increases distinctly. By increasing the CVD temperature to 500 °C, similarly, rough nanowire arrays ($MoSe_2$/CC) are still obtained as shown in Fig. S3. Hence, nanosheets are formed on the surface of the nanowire after selenation. After annealing the MoO_3/CC in the same atmosphere but without the Se precursor, the nanowire structure (MoO_2/CC) can still be observed as shown in Fig. S4.

TEM images in Fig. S5 and Fig. 1(d) confirm the nanosheet-nanowire core–shell structure of the CVD product with a core diameter of ~ 200 nm and a shell diameter of ~ 400 nm, in line with SEM analysis. The nanosheet structure is beneficial for active sites exposure for fast catalysis. Fig. 1(e) indicates firm integration between the nanowire core and nanosheet shell without sharp boundaries. Furthermore, HR-TEM image in Fig. 1(f) shows two sets of distinct lattice fringes with a neighbouring distance of 0.24 nm of the nanowire core ascribed to the MoO_2(–211) plane (JCPDS card No. 32–0671), whereas the lattice of 0.65 nm of the nanosheet shell belongs to the $MoSe_2$(002) plane (JCPDS card No. 77–1715). The elemental maps in Fig. 1(g) disclose the Mo-O core and Mo-Se shell in the as-prepared MSM. In addition, according to the atomic ratios of O and Se in the composite, the concentrations of $MoSe_2$ and MoO_2 in MSM are calculated to be 76.54% and 23.46%, respectively (Fig. S6).

XRD pattern in Fig. S7 shows that the product formed by the solution process is MoO_3 (JCPDS card No. 21–0569). After CVD

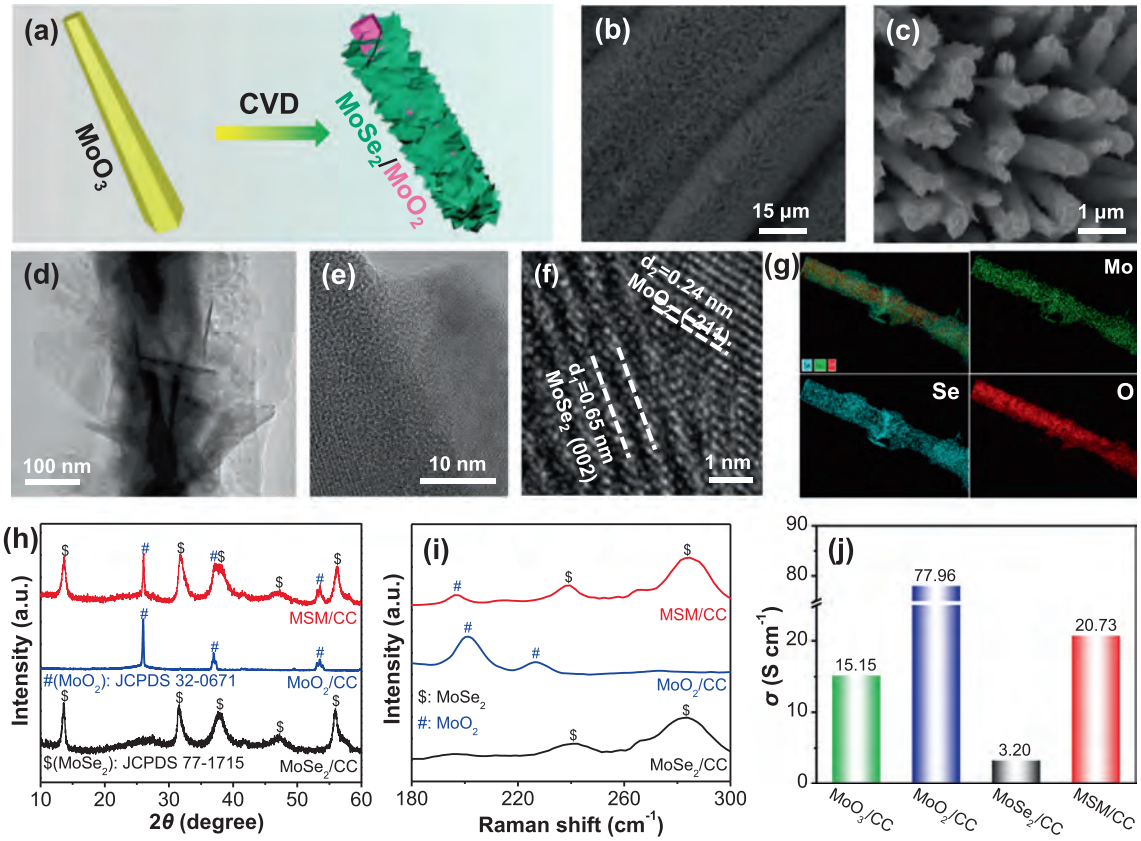

Fig. 1. (a) Schematic of the conversion of the MoO_3 nanowire into MSM core–shell structure. (b and c) FE-SEM, (d and e) TEM images, (f) HR-TEM image, and (g) elemental maps of MSM/CC. (h) XRD spectra, (i) Raman scattering spectra, and (j) conductivity of the electrocatalysts.

for selenation at 400 °C, Fig. 1(h) indicates that the diffraction patterns (red line) of the product belong to the composite of $MoSe_2$ (JCPDS card No. 77–1715) and MoO_2 (JCPDS card No. 32–0671). The results confirm that MoO_3 is phase-separated into the composite of $MoSe_2$ and MoO_2 during selenation. By increasing the selenation temperature to 500 °C, the pure phase of $MoSe_2$ (JCPDS card No. 77–1715) appears as shown in Fig. 1(h) (black line). By annealing MoO_3/CC at 550 °C for 3 h without the Se powder, the pure phase of MoO_2/CC (JCPDS card No. 32–0671) is formed as shown by the blue line in Fig. 1(h). Pure MoO_2 cannot be obtained at a lower annealing temperature (450 °C, 6 h) or in a shorter time duration (550 °C, 2 h) as shown in Fig. S8, suggesting that the Se powder is crucial to the conversion of MoO_3 into MoO_2. The products are investigated by Raman scattering as shown in Fig. 1(i), which confirms the composite of MoO_2 and 1*T*-$MoSe_2$ [38]. Fig. 1 (j) indicates that conversion from MoO_3/CC to MoO_2/CC improves the electrical conductivity, whereas the pure selenide $MoSe_2$/CC shows the lowest conductivity. It has been reported that 1*T*-$MoSe_2$ shows excellent electrocatalytic activity in HER [34] and therefore, combining the highly active 1*T*-$MoSe_2$ with a highly conductive skeleton may enhance the catalytic capability. The conductivity of the core–shell structure of MSM/CC is about six times larger than that of the pure phase $MoSe_2$/CC as well as superior to the MoO_3/CC precursor, as indicated in Fig. 1(j). The synergetic effects of high active site exposure and conductivity of the MSM/CC composite are expected to benefit HER.

The chemical composition of the electrocatalysts was investigated by XPS. The selenide products including MSM/CC and $MoSe_2$/CC show the presence of Se in the surface survey in Fig. S9. The high-resolution XPS spectra of Se 3*d* in Fig. S10(a and b) show similar spectra for the selenide samples and the peaks located at 55.7/54.8 eV are Se^{2-} $3d_{3/2}/3d_{5/2}$. However, the Mo 3*d* spectra of MSM/CC, MoO_2/CC and $MoSe_2$/CC are different as shown in Fig. S11. MoO_2/CC is composed of Mo^{4+} (233.2 and 230.0 eV) and Mo^{6+} (235.6 and 232.1 eV) as shown by the Mo 3*d* spectra (Fig. S11a). The presence of Mo^{6+} in MoO_2/CC stems from surface oxidation in the air as reported before [39]. Fig. S11(b and c) shows that the Mo 3*d* peak in MSM/CC and $MoSe_2$/CC is composed of Mo^{4+} $3d_{3/2}$ and $3d_{5/2}$. The Mo^{4+} peaks in MSM/CC are shifted ~ 0.56 eV lower compared to MoO_2/CC, but ~ 0.20 eV higher than $MoSe_2$/CC. The peak shifts reveal the electronic interaction between the MoO_2 and $MoSe_2$ phases at the MSM heterointerface [13,25].

3.2. HER performance of the catalysts

The electrochemical properties of the electrocatalysts were studied systematically based on the three-electrode configuration. Fig. 2(a) depicts the polarization curves of the electrocatalysts in the alkaline electrolyte (1.0 M KOH) for HER. The MSM/CC electrocatalyst requires only 181 mV for a current density of 10 mA cm^{-2}, which is a common criterion to evaluate the activity of water splitting. The overpotential of the MSM/CC electrocatalyst is smaller than those of the pure phase of $MoSe_2$/CC (216 mV), MoO_2/CC (358 mV) and MoO_3/CC (363 mV), as listed in Table S1. Moreover, the MSM/CC electrocatalyst exhibits a rapid rise in the current density and an overpotential of 449 mV is required to generate a large current density of 500 mA cm^{-2}. Fig. 2(b) shows the Tafel plots of the electrocatalysts. The smallest Tafel slope of 110.4 mV dev^{-1} is observed from the MSM/CC electrocatalyst compared to the pure phase of $MoSe_2$/CC (133.6 mV dev^{-1}), MoO_2/CC (117.6 mV dev^{-1}), and MoO_3/CC (385.8 mV dev^{-1}). A smaller Tafel slope normally implies faster mass transport and charge transfer, which can be

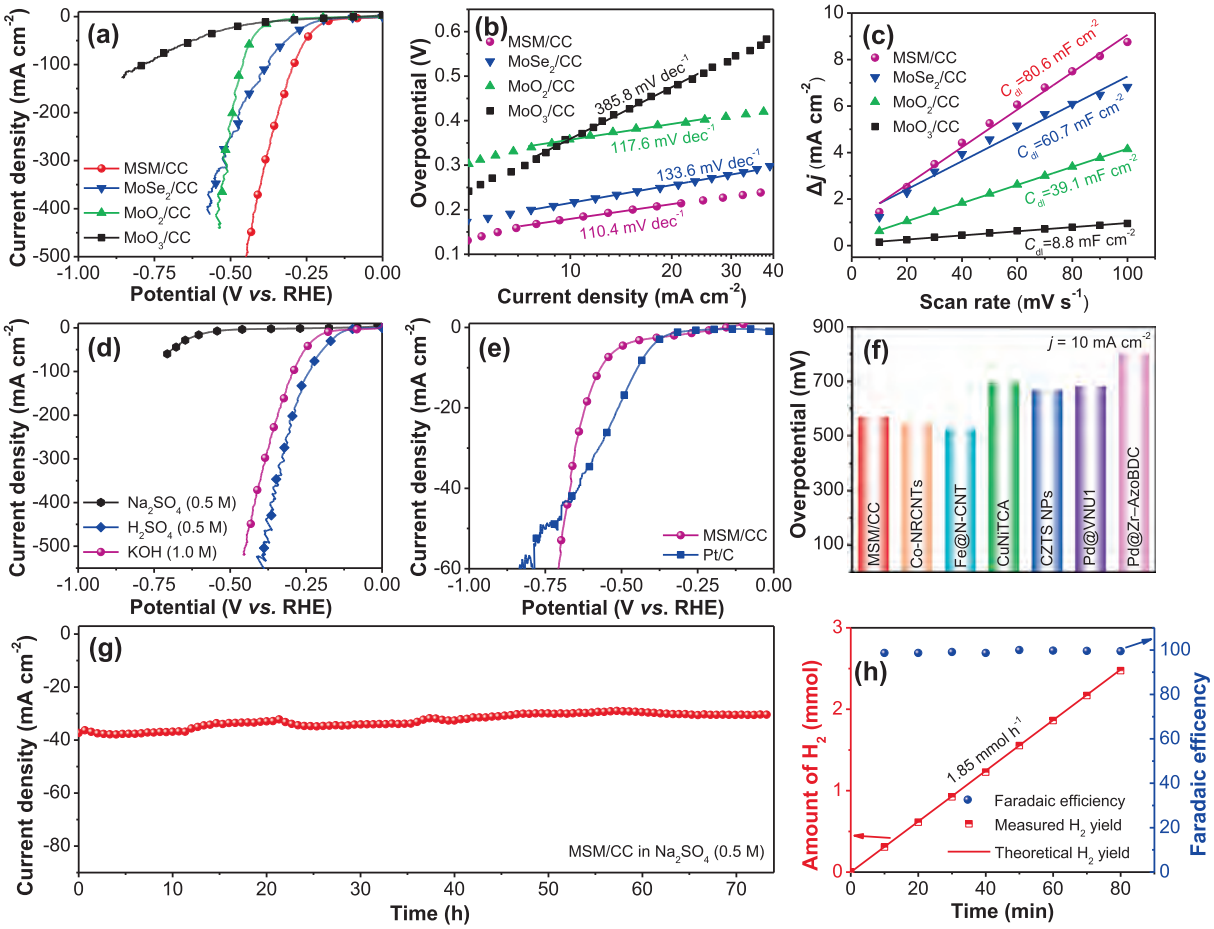

Fig. 2. (a) LSV curves, (b) Tafel plots, (c) ECSA of the electrocatalysts measured in 1.0 M KOH electrolyte. (d) LSV curves of the MSM/CC electrocatalyst in different electrolytes. (e) LSV curves of MSM/CC and commercial Pt/C electrocatalysts in 0.5 M Na_2SO_4. (f) Comparison of the overpotentials of MSM/CC with those of previously reported electrocatalysts in neutral electrolytes. (g) Stability of MSM/CC in 0.5 M Na_2SO_4. (h) Experimental and theoretical amounts of H_2 produced by the MSM/CC electrocatalyst and Faradaic efficiency at 100 mA.

confirmed by EIS in Fig. S12. The smaller charge transfer resistance of MSM/CC suggests fast charge transfer during HER due to the tight combination of the highly active $MoSe_2$ shell and highly conductive MoO_2 core.

Density-functional theory calculation (Supporting Note 1) was performed to elucidate the mechanism of the MSM/CC heterostructure. The simulated model for the MSM composed of $MoSe_2$(002) and MoO_2(−211) heterointerface is depicted in Fig. S13(a). The calculated ΔG_H of $MoSe_2$, MoO_2, and MSM heterointerface was adopted to estimate the hydrogen evolution activity, as shown in Fig. S13(b). MSM shows a ΔG_H of −0.18 eV which is closer to zero compared to pure $MoSe_2$ (−0.24 eV) and MoO_2 (0.54 eV), indicating that the interaction between $MoSe_2$ and MoO_2 at the heterointerface modulate the electronic structure of the active centers to accelerate HER consistent with the XPS result.

The ECSA was derived to evaluate active site exposure based on cyclic voltammetry (Fig. S14). The larger the ECSA, the greater the active site exposure. As shown in Fig. 2(c), the MSM/CC electrocatalyst has the largest ECSA of 80.6 mF cm^{-2}, which is about 10 times that of the MoO_3/CC precursor, suggesting more active site exposure after CVD for phase separation. The results are supported by the SEM images after selenation showing that the surface of the nanowire becomes rough and sheet-like so that more active sites are exposed. The smaller overpotential, Tafel slope, and charge transfer resistance, as well as the larger ECSA of the MSM/CC electrocatalyst, confirm the promotional effect of the $MoSe_2$ and MoO_2 heterostructure. The outstanding HER performance can be ascribed to the modulated electronic structure of the heterointerface between the two phases and the synergistic effects of highly active $MoSe_2$ and conductive MoO_2.

The HER capability of the MSM/CC electrocatalyst in electrolytes with a universal pH range was investigated and shown in Fig. 2(d) and Fig. S15 and the overpotentials and Tafel slopes are listed in Table S2. In an acidic electrolyte (0.5 M H_2SO_4), the hydrated hydrogen ions serve as proton donors to achieve a fast Volmer step [40], so that the smaller overpotential (132 mV at 10 mA cm^{-2}) and Tafel slope (68.6 mV dec^{-1}) are realized and they are superior to those of other $MoSe_2$-based electrocatalysts in the literature (Fig. S16). The HER performance of the MSM/CC electrocatalyst in a neutral electrolyte (0.5 M Na_2SO_4) was studied and an overpotential of 568 mV was required for 10 mA cm^{-2}, together with a Tafel slope of 174.6 mV dec^{-1}. Generally, the HER characteristics in neutral media are inferior to those in acidic and alkaline media. However, it is more practical to produce hydrogen in neutral electrolytes since it can avoid the use of undesirable strong acids or bases, which could eliminate environmental and handling problems and less electrode damage and equipment corrosion [41]. The MSM/CC electrocatalyst shows a more rapid rise in the current density throughout the applied potential range than the commercial Pt/C catalyst, as indicated in Fig. 2(e). The overpotentials required to produce current densities beyond 45 mA cm^{-2} are even smaller compared to the commercial Pt/C catalyst. The HER

characteristics of the MSM/CC electrocatalyst and other typical transition metal-based electrocatalysts including Fe@N-CNT [17], CuNiTCA [42], Co-NRCNTs [43], CZTS NPs [44], Pd@VNU1 [45], Pd@Zr-AzoBDC [46] in neutral electrolytes are compared in Fig. 2 (f) and the former indeed delivers outstanding performance.

Fig. 2(g) shows the stability of the MSM/CC electrocatalyst in the neutral electrolyte and the catalyst worked stably for more than 75 h without obvious decay in the current density. Moreover, the morphology of the MSM/CC electrocatalyst remains the same with the nanosheets cover the nanowire arrays (Fig. S17). Fig. S18 shows similar diffraction patterns from the MSM/CC electrocatalyst after a long-term test, compared to the fresh one, implying the high stability of MSM/CC. The amount of H_2 produced by the MSM/CC electrocatalyst in HER under the neutral condition is measured by the water displacement configuration as schematically illustrated in Fig. S19. The volume of hydrogen collected is determined by a measuring cylinder (100 mL) and 60.5 mL of hydrogen is produced after HER for 80 min at a constant current of 100 mA. High-purity hydrogen is emitted from the neutral electrolyte at a fast rate of 1.85 mmol h^{-1} (Fig. 2h). In addition, the Faradaic efficiency is calculated to be as high as 99.58% (Supporting Note 2) corroborating the high efficiency in the neutral media.

3.3. FUR and overall reaction performance

Since Fe corrodes easily and even self-corrodes in the electrolyte, during which both the anodic and cathodic reactions will occur spontaneously at the electrode surface, and as a result, the electrode potential will be different from the reversible or equilibrium potential of each reaction occurring at the surface [47]. In this case, the corrosion potential of Fe is intermediate between the equilibrium potential of the two half-reactions, as indicated by the corrosion potential (–0.29 V *vs.* RHE) measurement in Fig. S20. Iron-based species have been investigated as OER electrocatalysts and reconstruction by oxidizing to higher valence states occurs before OER [48,49]. That is, the FUR is more thermodynamic favourable than OER. More importantly, waste steel in the construction industry can be recycled to be used as Fe electrodes instead of fresh smelting to reduce the cost, energy consumption, and carbon emission. Here, a waste steel rod (Fig. S21) is used as the Fe electrode to determine the FUR properties. The polarization curve in Fig. 3(a) shows that merely 0.11 V *vs.* RHE is required to generate a current density of 10 mA cm^{-2} in FUR in the neutral electrolyte (0.5 M Na_2SO_4), which is 2.01 V smaller than that in OER and even 1.71 V smaller than that of the commercial IrO_2 electrocatalyst (Fig. 3a and Fig. S22). The results show that by replacing OER with FUR, the potential required to achieve a current density of 10 mA cm^{-2} can decrease by 95%. During FUR, white flocculent precipitates are formed as shown in Fig. S23(a). To analyze the product of FUR, the final electrolyte after FUR was put in a $KMnO_4$ aqueous solution. The purple $KMnO_4$ solution turns into a clay bank as shown in Fig. S23(b and c), suggesting that Fe^{2+} is produced in FUR by electrochemical oxidation of the Fe electrode, which agrees with the literature [17]. The results predict that combining HER and FUR can give rise to energy-saving hydrogen production with hydrogen being the only gaseous product.

To assess the practicability of the HER/FUR strategy for hydrogen production, the overall reaction of HER and FUR using the MSM/CC electrocatalyst and waste steel rod as electrodes was carried out, as schematically illustrated in Fig. 3(b). The polarization curve acquired in the neutral electrolyte (0.5 M Na_2SO_4) is presented in Fig. 3(c). The voltage required by the MSM/CC||Fe couple is smaller than that of the commercial Pt/C||IrO_2 couple. In detail, a voltage of 0.68 V is needed to generate a current density of 10 mA cm^{-2} for the MSM/CC||Fe couple in the neutral electrolyte and it is superior to those of the HER/OER and other couples in acidic and basic electrolytes, as listed in Table S3. The faradaic efficiency of the HER/FUR overall configuration for H_2 production was calculated to be 99.5% in an electrolyzer without a separator as shown in Fig. S24(a and b), which suggested that the reactants and products of the redox reactions occurring on the cathode and anode do not interact with each other. The evaluation of the stability and feasibility of the HER/FUR integrated system in Fig. S25 shows a slight decay of the current density after continuous testing for 24 h, which can be ascribed to the consumption of the Fe anode since the current density returns to the initial state after Fe electrode replacement. The precipitated floccule (after washing and drying) formed in HER/FUR was studied by FE-SEM and XRD revealing nanosized Fe_3O_4 (JCPDS card No. 75–0033) particles (Fig. 3d and Fig. S26), resulting from partial oxidation of Fe^{2+} since it is generally unstable and prefers to be oxidized [50]. Moreover, the magnetic properties of the as-obtained Fe_3O_4 nanoparticles and commercial Fe_3O_4 (purchased from Tianjin Zhiyuan Chemical Reagent Co. Ltd.) were investigated and shown in Fig. 3(e). The as-obtained Fe_3O_4 nanoparticles and commercial Fe_3O_4 particles have magnetic saturation values of approximately 52.0 and 2.6 emu g^{-1}, respectively, suggesting superior magnetic properties for the as-obtained Fe_3O_4 nanoparticles. In addition, the final Fe product can be picked up by a magnet as shown in the inset in Fig. 3(e), suggesting promising magnetic applications. Generally, the nanosized magnetic powder is more valuable than the waste steel rod at the anode and therefore, the anodic reaction is value-adding and could further reduce the cost of hydrogen production. Furthermore, the electricity equivalent for the HER/FUR couple in the neutral electrolyte is calculated to be 2.69 kWh per m^3 H_2 (Supporting Note 3). More importantly, high-purity hydrogen and value-adding Fe_3O_4 nanoparticles are produced in conjunction with zero carbon emission. It is lower than that of common overall water splitting systems including Ni-P-B/Ni foam [51], CDs/CoP/NF [52], CoSAs-MoS_2/TiN NRs [53], CoS_x||Co_9S_8 [54], FeMn-MOF/NF (1:1) [55], HP-TiO_2/Ni foam [56], LIA-Ni-BDC||LIA-MIL-101(Fe) [57], Ni_3S_2/NF||Ni_3S_2/NF [58], N-Ni_3S_2/NF [59], and even less than the theoretical limit of conventional overall water splitting (2.94 kWh per m^3 H_2), as shown in Fig. 3(f).

3.4. RhB beneficiation

Coupling FUR and HER enables energy-saving hydrogen production and value-adding by-products but FUR consumes Fe. To further increase the economic benefits of HER/FUR, the product can be used to extract RhB from polluted water via flocculation. After adding RhB (0.5 mM) into the neutral electrolyte, the polarization curves for the HER and FUR remain the same, as shown in Fig. S27. During the HER/FUR overall reaction, the colour of the electrolyte (100 mL) changes from rose red to garnet accompanied by floccule formation. The electrolyte then turns colourless and precipitates are formed as shown in Fig. S28. The precipitation process is shown in the Supporting Video which shows that bubbles are emitted from the cathode and floccule precipitates in the electrolyte in HER/FUR.

Fig. 4(a) shows the scheme for the treatment of wastewater and the formation of value-adding products. RhB-containing wastewater can be purified by the HER/FUR overall reaction, as indicated by the fact that the TOC decreases from 167.9 to 19.5 mg L^{-1} (Fig. S29). The UV–vis spectra of the electrolyte during the overall reaction are shown in Fig. 4(b), which indicates that RhB can be completely removed after the reaction for ~ 30 min as indicated by the characteristic peak of RhB at ~ 554 nm [60]. After filtration of the floccule, RhB is released and redissolved in DW (40 mL) via coagulation of Fe species in hot water (80 °C) bath for 30 min. The UV–vis spectrum of the regenerated electrolyte exhibits the same peak as the initial one, as shown in Fig. 4(c). However, the

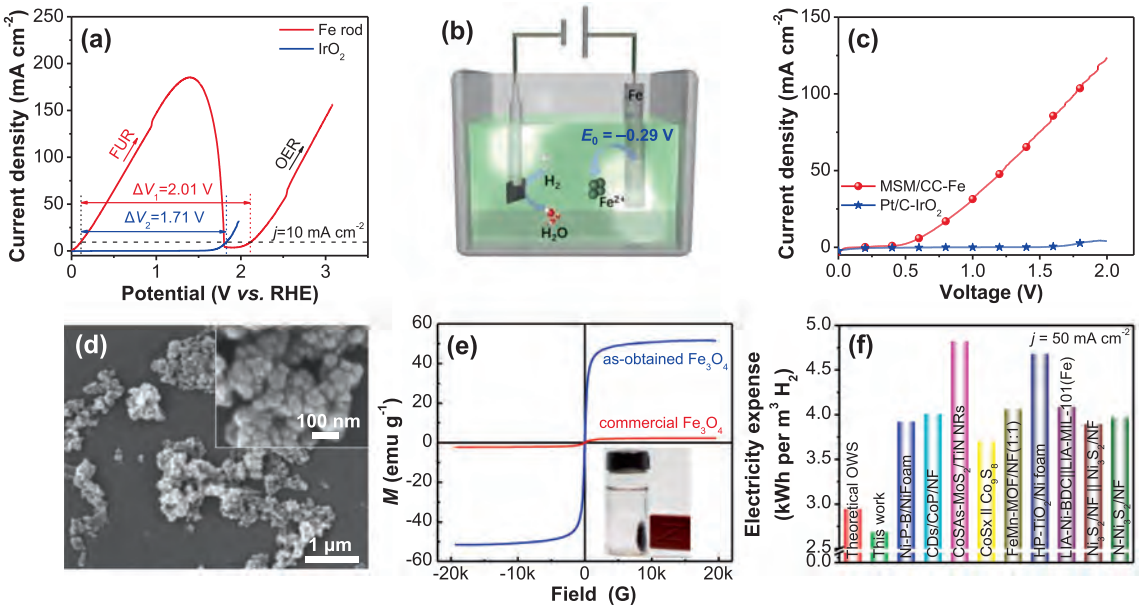

Fig. 3. (a) LSV curves of FUR with a waste steel rod as the working electrode. (b) Model of the HER/FUR couple. (c) LSV curves of MSM/CC||Fe and Pt/C||IrO_2 couples. (d) SEM images and (e) magnetic properties of the as-obtained Fe_3O_4. (f) Comparison of the energy requirement of the HER/FUR overall reaction system in this work with those of theoretical overall water splitting and reported works.

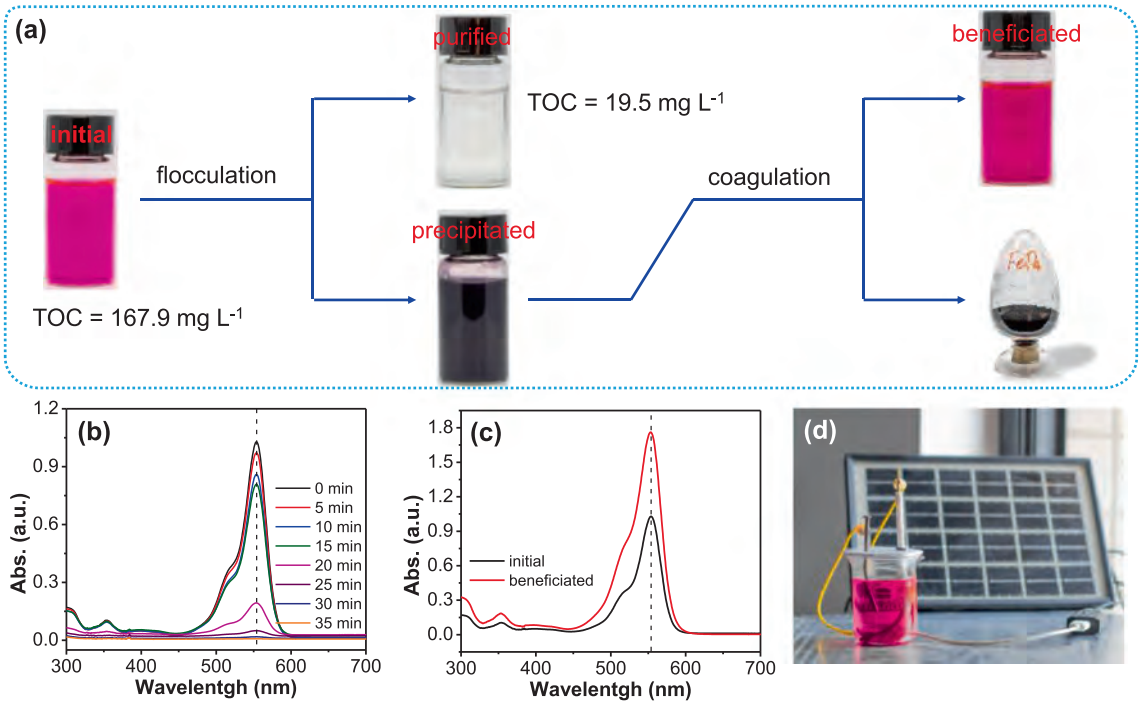

Fig. 4. (a) Scheme for wastewater recovery and formation of value-adding products. (b) UV–vis spectra of the electrolyte (6 times dilution) during the HER/FUR overall reaction. (c) UV–vis spectra of the fresh electrolyte and beneficiated RhB with 6 times dilution. (d) Photograph showing the solar cell-powered HER/FUR overall reaction system.

absorbance increases by 80% revealing that a higher concentration of RhB is obtained. The FT-IR spectra of commercial RhB, initial RhB in the electrolyte, and the final beneficiated RhB are obtained and presented in Fig. S30. RhB is extracted from the solution by drying, ethanol dissolution, filtration, and drying again to remove water, salts, and Fe species before conducting FT-IR. The results show that all the characteristic peaks from both the initial RhB in the electrolyte and the final beneficiated RhB are the same as those of commercial RhB. After the release of RhB, the final Fe species are determined to be Fe_3O_4 despite the floccule with low crystallinity (Fig. S31). It may stem from that absorption of RhB around the Fe species slowing down crystallization. The results reveal that the chemistry of RhB remains unchanged through floccule precipitation, during which RhB can be beneficiated without carbon

emission. Furthermore, the HER/FUR overall reaction can be powered by a solar cell with an output voltage of 1.5 V as illustrated in Fig. 4(d). Bubbles are generated from the MSM/CC electrode only as shown in Fig. S32(a and b). The results indicate that energy-saving hydrogen production can be realized in conjunction with RhB beneficiation from wastewater in one system powered by sustainable energy.

The RhB beneficiation process and mechanism are discussed. Firstly, the steel rod is oxidized into Fe^{2+} on the anode during the reaction. Owing to the small K_{sp} (solubility product constant) of $Fe(OH)_2$, Fe^{2+} prefers to form $Fe(OH)_2$ precipitate in the neutral electrolyte (0.5 M Na_2SO_4, pH = 5.80) as described in the Supporting Note 4. Secondly, the RhB molecules adsorb onto the $Fe(OH)_2$ and precipitate with it. As a result, RhB is extracted from the polluted electrolyte and the resulting concentration diminishes. Generally, Fe^{2+} is unstable and prefers to be oxidized. Thirdly, by means of the separation of $Fe(OH)_2$ and RhB by coagulation in the hot water bath (80 °C) for 30 min, the adsorbed RhB is released into the solution to form a beneficiated solution for reuse. At the same time, $Fe(OH)_2$ is precipitated and sinks to the bottom. In the full cycle of absorption and release of the RhB, only electrostatic adsorption works and therefore, RhB can be beneficiated without chemical evolution. Therefore, the FUR coupled HER overall reaction not only decreases the energy consumption of hydrogen production intrinsically but also beneficiates RhB from wastewater for recycling. Moreover, magnetic Fe_3O_4 nanoparticles are produced from the waste steel rod, as analyzed in Supporting Note 5. The process accomplishes clean energy production and environmental recovery at the same time while emitting zero carbon.

4. Conclusions

A strategy of integrating HER and FUR is demonstrated for energy-saving hydrogen production and simultaneous organic pollutant removal/recovery in neutral wastewater. The synergetic effects of exposure of large active sites of the core/shell structure, high conductivity of the MoO_2 core, as well as electronic interaction between Ni and Mo atoms at the MSM/CC heterointerface give rise to small overpotentials and fast kinetics in HER for the heterostructured MSM/CC electrocatalyst in the neutral electrolyte. In addition, the morphology and structure of the electrocatalyst remain unchanged after continuous measurement for 75 h thereby providing evidence about the outstanding long-term stability. The potential required to achieve a current density of 10 mA cm^{-2} in FUR decreases by 95% compared to OER as a result of the favorable thermodynamics of FUR. Our results indicate that the waste steel rod at anode is oxidized into Fe^{2+} and finally converted into value-adding Fe_3O_4 magnetic nanoparticles. The produced Fe species on the anode serve as absorbents to flocculate RhB from wastewater and the Fe species are then separated from the floccule to beneficiate RhB. The strategy demonstrated in this work is appropriate for removing and beneficiating other heavy metal ions and organic species, which has practical significance. The results also reveal a novel strategy to realize energy-efficient hydrogen production and environmental recovery at the same time and in particular, the technique is promising for carbon–neutral energy and ecological systems.

Declaration of competing interest

The authors declare that they have no known competing financial interests or personal relationships that could have appeared to influence the work reported in this paper.

Acknowledgments

This work was financially supported by the Key Research and Development Program of Hubei Province (2021BAA208), the National Natural Science Foundation of China (52002294, 51974208 and U2003130), the Young Top-notch Talent Cultivation Program of Hubei Province, Knowledge Innovation Program of Wuhan-Shuguang Project (2022010801020364), the City University of Hong Kong Strategic Research Grant (SRG) (7005505), and the City University of Hong Kong Donation Research Grant (DON-RMG 9229021). The authors would like to thank Hongyu Wang from Shiyanjia Lab (www.shiyanjia.com) for the magnetic saturation measurement and analysis.

Appendix A. Supplementary material

Supplementary data to this article can be found online at https://doi.org/10.1016/j.jechem.2023.03.022.

References

[1] H. Wu, C. Feng, L. Zhang, J. Zhang, D.P. Wilkinson, Electrochem. Energy R. 4 (2021) 473–507.
[2] X.W. Fu, R.J. Shi, S.L. Jiao, M.M. Li, Q.Y. Li, J. Energy Chem. 70 (2022) 129–153.
[3] Y. Xu, R.Y. Ge, J. Yang, J.C. Li, S. Li, Y. Li, J.J. Zhang, J. Feng, B. Liu, W.X. Li, J. Energy Chem. 74 (2022) 45–71.
[4] F. Zhou, Y. Zhou, G. Liu, C. Wang, J. Wang, Rare Met. 40 (2021) 3375–3405.
[5] B. Zhang, L. Wang, Z. Cao, S.M. Kozlov, F.P. García de Arquer, C.T. Dinh, J. Li, Z. Wang, X. Zheng, L. Zhang, Nat. Catal. 3 (2020) 985–992.
[6] G.A. Gebreslase, M.V. Martinez-Huerta, M.J. Lazaro, J. Energy Chem. 67 (2022) 101–137.
[7] J. Li, C. Zhang, C. Zhang, H. Ma, Z. Guo, C. Zhong, M. Xu, X. Wang, Y. Wang, H. Ma, Adv. Mater. 34 (2022) 2203900.
[8] Y. Li, J. Zhang, Y. Liu, Q. Qian, Z. Li, Y. Zhu, G. Zhang, Sci. Adv., 6 (2020) eabb4197.
[9] H. Zhao, D. Lu, J. Wang, W. Tu, D. Wu, S.W. Koh, P. Gao, Z.J. Xu, S. Deng, Y. Zhou, Nat. Commun. 12 (2021) 2008.
[10] T. Wang, L. Tao, X. Zhu, C. Chen, W. Chen, S. Du, Y. Zhou, B. Zhou, D. Wang, C. Xie, Nat. Catal. 5 (2022) 66–73.
[11] Q. Qian, J. Zhang, J. Li, Y. Li, X. Jin, Y. Zhu, Y. Liu, Z. Li, A. El-Harairy, C. Xiao, G. Zhang, Y. Xie, Angew. Chem. Int. Ed. 60 (2021) 5984–5993.
[12] L. Zhang, Z. Wang, J. Qiu, Adv. Mater. 34 (2022) 2109321.
[13] F. Sun, J. Qin, Z. Wang, M. Yu, X. Wu, X. Sun, J. Qiu, Nat. Commun. 12 (2021) 4182.
[14] X. Peng, Y. Yan, X. Jin, C. Huang, W. Jin, B. Gao, P.K. Chu, Nano Energy 78 (2020).
[15] Z.L. Cheng, Y.X. Li, Z. Liu, J. Alloys Compd. 708 (2017) 255–263.
[16] M. Hasanpour, M. Hatami, J. Mol. Liq. 309 (2020).
[17] J. Yu, G. Li, H. Liu, L. Zeng, L. Zhao, J. Jia, M. Zhang, W. Zhou, H. Liu, Y. Hu, Adv. Sci. 6 (2019) 1901458.
[18] Z. Zhang, S. Chen, Y. Li, S. Li, L. Wang, Corros. Sci. 51 (2009) 291–300.
[19] I.T. McCrum, M. Koper, Nat. Energy 5 (2020) 891–899.
[20] K.L. Zhou, Z. Wang, C.B. Han, X. Ke, C. Wang, Y. Jin, Q. Zhang, J. Liu, H. Wang, H. Yan, Nat. Commun. 12 (2021) 1–10.
[21] Y. Wang, R. Li, H. Li, L. Huang, Z. Guo, H. Chen, Y. Zheng, K. Qu, Rare Met. 40 (2021) 1040–1047.
[22] S.S. Niu, J. Yang, H.F. Qi, Y. Su, Z.Y. Wang, J.S. Qiu, A.Q. Wang, T. Zhang, J. Energy Chem. 57 (2021) 371–377.
[23] C.R. Zhu, D. Gao, J. Ding, D. Chao, J. Wang, Chem. Soc. Rev. 47 (2018) 4332–4356.
[24] W. Liu, P. Geng, S.Q. Li, W.H. Liu, D.Y. Fan, H.D. Lu, Z.H. Lu, Y.P. Liu, J. Energy Chem. 55 (2021) 17–24.
[25] X. Peng, A.M. Qasim, W. Jin, L. Wang, L. Hu, Y. Miao, W. Li, Y. Li, Z. Liu, K. Huo, K.-Y. Wong, P.K. Chu, Nano Energy 53 (2018) 66–73.
[26] J. Ye, Y. Zang, Q. Wang, Y. Zhang, D. Sun, L. Zhang, G. Wang, X. Zheng, J. Zhu, J. Energy Chem. 56 (2021) 283–289.
[27] W.J. Xie, K. Liu, G.D. Shi, X.L. Fu, X.J. Chen, Z.X. Fan, M. Liu, M.J. Yuan, M. Wang, J. Energy Chem. 60 (2021) 272–278.
[28] W. Zang, T. Sun, T. Yang, S. Xi, M. Waqar, Z. Kou, Z. Lyu, Y.P. Feng, J. Wang, S.J. Pennycook, Adv. Mater. 33 (2021) 2003846.
[29] X. Peng, C. Pi, X. Zhang, S. Li, K. Huo, P.K. Chu, Sustain. Energ. Fuels 3 (2019) 366–381.
[30] X. Peng, Y. Yan, S. Xiong, Y. Miao, J. Wen, Z. Liu, B. Gao, L. Hu, P.K. Chu, J. Mater. Sci. Technol. 118 (2022) 136–143.
[31] X. Peng, S. Xie, X. Wang, C. Pi, Z. Liu, B. Gao, L. Hu, W. Xiao, P.K. Chu, J. Mater. Chem. A 10 (2022) 20761–20769.
[32] B. Xia, T. Wang, X. Jiang, T. Zhang, J. Li, W. Xiao, P. Xi, D. Gao, D. Xue, J. Ding, ACS Energy Lett. 3 (2018) 2167–2172.
[33] C.H. An, W. Kang, Q.B. Deng, N. Hu, Rare Met. 41 (2022) 378–384.
[34] L. Chang, Z. Sun, Y.H. Hu, Electrochem. Energy R. 4 (2021) 194–218.

[35] L. Xiong, Y. Qiu, X. Peng, Z. Liu, P.K. Chu, Nano Energy 104 (2022).
[36] Y. Qu, H. Medina, S.W. Wang, Y.C. Wang, C.W. Chen, T.Y. Su, A. Manikandan, K. Wang, Y.C. Shih, J.W. Chang, Adv. Mater. 28 (2016) 9831–9838.
[37] S. Deng, C. Ai, M. Luo, B. Liu, Y. Zhang, Y. Li, S. Lin, G. Pan, Q. Xiong, Q. Liu, Small 15 (2019) 1901796.
[38] U. Gupta, B. Naidu, U. Maitra, A. Singh, S.N. Shirodkar, U.V. Waghmare, C. Rao, APL Mater. 2 (2014).
[39] X.F. Lu, Z.X. Huang, Y.X. Tong, G.R. Li, Chem. Sci. 7 (2016) 510–517.
[40] P. Li, Y. Jiang, Y. Hu, Y. Men, Y. Liu, W. Cai, S. Chen, Nat. Catal. 5 (2022) 900–911.
[41] Z.Y. Yu, Y. Duan, X.Y. Feng, X. Yu, M.R. Gao, S.H. Yu, Adv. Mater. 33 (2021) 2007100.
[42] R.S. Vishwanath, S. Kandaiah, J. Mater. Chem. A 5 (2017) 2052–2065.
[43] X. Zou, X. Huang, A. Goswami, R. Silva, B.R. Sathe, E. Mikmeková, T. Asefa, Angew. Chem. Int. Ed. 53 (2014) 4372–4376.
[44] R.V. Digraskar, B.B. Mulik, P.S. Walke, A.V. Ghule, B.R. Sathe, Appl. Surf. Sci. 412 (2017) 475–481.
[45] H.V. Le, T.H. Le Doan, B.Q. Tran, H.H.T. Nguyen, T.T. Co, H.T. Nguyen, N.T. Le Huynh, L.P.T. Nguyen, M. Van Tran, Mater. Chem. Phys. 233 (2019) 16–20.
[46] H.V. Le, Q.T.T. Nguyen, T.T. Co, P.K.T. Nguyen, H.T. Nguyen, J. Electron. Mater. 47 (2018) 6918–6922.
[47] X. Cheng, I. Iwasaki, Miner. Process. Extr. Metall. Rev. 11 (1992) 187–210.
[48] L. Fan, B. Zhang, B.J.J. Timmer, N.V.R.A. Dharanipragada, X. Sheng, C.-W. Tai, F. Zhang, T. Liu, Q. Meng, A.K. Inge, L. Sun, Nano Energy 72 (2020).
[49] F. Yang, X. Chen, Z. Li, D. Wang, L. Liu, J. Ye, ACS Appl. Energy Mater. 3 (2020) 3577–3585.
[50] R. Chen, C. Yin, H. Liu, Y. Wei, J. Mol. Catal. A: Chem. 397 (2015) 114–119.
[51] W. Hao, R. Wu, H. Huang, X. Ou, L. Wang, D. Sun, X. Ma, Y. Guo, Energy Environ. Sci. 13 (2020) 102–110.
[52] L.C. Zhang, H. Chen, G.R. Hou, L.Z. Zhang, Q.L. Li, Y.K. Wu, M. Xu, S.J. Bao, Chem. Commun. 56 (2020) 257–260.
[53] T.L.L. Doan, D.C. Nguyen, S. Prabhakaran, D.H. Kim, D.T. Tran, N.H. Kim, J.H. Lee, Adv. Funct. Mater. 31 (2021) 2100233.
[54] R. Souleymen, Z. Wang, C. Qiao, M. Naveed, C. Cao, J. Mater. Chem. A 6 (2018) 7592–7607.
[55] H. Guan, N. Wang, X. Feng, S. Bian, W. Li, Y. Chen, Colloids Surf., A 624 (2021).
[56] Y. Yan, X. Cheng, W. Zhang, G. Chen, H. Li, A. Konkin, Z. Sun, S. Sun, D. Wang, P. Schaaf, ACS Sustain. Chem. Eng. 7 (2018) 885–894.
[57] Y.J. Tang, H. Zheng, Y. Wang, W. Zhang, K. Zhou, Adv. Funct. Mater. 31 (2021) 2102648.
[58] X. Luo, P. Ji, P. Wang, R. Cheng, D. Chen, C. Lin, J. Zhang, J. He, Z. Shi, N. Li, Adv. Energy Mater. 10 (2020) 1903891.
[59] P. Chen, T. Zhou, M. Zhang, Y. Tong, C. Zhong, N. Zhang, L. Zhang, C. Wu, Y. Xie, Adv. Mater. 29 (2017) 1701584.
[60] D. Chen, J. Ye, Adv. Funct. Mater. 18 (2008) 1922–1928.

Supporting Information

Ultralow-voltage hydrogen production and simultaneous Rhodamine B beneficiation in neutral wastewater

Supporting Note 1. Density-functional theory calculation

Density-functional theory (DFT) calculation is performed using the DMol3 program implemented in Material Studio [1] and the slab model with a vacuum space of 15 Å along the z-direction is adopted. The $MoSe_2$ (002) and MoO_2(−211) surfaces are selected in the model based on the lattice revealed by HR-TEM. The exchange-correlation functional under the generalized gradient approximation (GGA) within the Perdew-Burke-Ernzerhof (PBE) functional is implemented [2]. The double-numeric (DN) quality basis set is adopted and the core electrons are treated with the DFT semi-core pseudopotentials (DSPPs) [3, 4]. The convergence tolerance of optimal configuration for the energy, force, and maximum displacement is 1.0×10^{-5} Ha, 0.002 Ha/Å, and 0.005 Å, respectively.

The reaction free energy correction is calculated according to the following equation [5]:

$$\Delta G = \Delta E + \Delta ZPE + \Delta H - T\Delta S, \quad \text{(Equation S1)}$$

where ΔE, ΔZPE, ΔH, and ΔS refer to the reaction energy from the DFT calculation, change of zero-point energy, integrated heat capacity from 0 K to 298.15 K, and entropy change, respectively. The adsorption energy (E_{ads}) of the intermediates (int.) on the surface of the substrate is defined as:

$$E_{ads} = E_{*int.} - (E_{*} + E_{int.}), \quad \text{(Equation S2)}$$

where *int. and * denote adsorbed intermediates on the sample and bare substrate and $E_{int.}$ denotes the energy of individual intermediates [6].

Supporting Note 2. Faradaic efficiency calculation

According to the water replacement measurement, 60.5 mL H_2 are produced in 80 min during HER at a current density of 100 mA cm^{-2} and room temperature (25 ºC). The geometrical area of the electrode is 1 cm^2.

(i) In this duration, the amount of hydrogen theoretically is:

$n(H_2)_T = i \times t / 2 \times F$ = (0.1 A × 80 min × 60 s) / (2 × 96485 C mol^{-1}) = 2.48743×10^{-3} mol, where $n(H_2)_T$ is the molar mass of total hydrogen produced in theory, i is current, t is the time duration, and F is Faraday's constant.

(ii) Under the experimental conditions (p = 101.325 KPa, T = 298 K), the molar volume of gas (V_m) is 24.45 L moL^{-1}. Thus, the measured hydrogen can be calculated by: $n(H_2)_M = V / V_m$ = 60.5 mL / 24.45 L mol^{-1} = 2.47444 × 10^{-3} mol, where $n(H_2)_M$ is the molar mass of the measured hydrogen and V is the volume of the produced hydrogen.

(iii) The Faradaic efficiency can be calculated as follows: $\eta = (n(H_2)_M / n(H_2)_T) \times 100\%$ = 99.58%

Supporting Note 3. Electricity equivalent calculation

According to the polarization curve in Fig. 3c, I = 0.05 A and U = 1.226V (close to the theoretical voltage for conventional overall water splitting) are used to calculate the energy equivalent: I = 0.05 A, U = 1.226 V. To produce 1 m^3 of hydrogen, the energy equivalent can be calculated as follows: $W = U \times I \times t = U \times I \times V/v$ = 1.226 V × 0.05 A × 1 m^3 / (2.28 × 10^{-5} m^3 h^{-1}) = 2.69 kWh, where W is the electricity, t is the time needed, V is the total volume of hydrogen, and v is the production rate of hydrogen under the experimental conditions. Therefore, the electricity equivalent of the HER/FUR system in this work is calculated to be 2.69 kWh per m^3 H_2. In comparison, the theoretical electricity requirement for conventional overall water splitting is 2.94 kWh per m^3 H_2.

Supporting Note 4. FUR mechanism

The possible reactions on the Fe anode are expressed as follows:

$Fe - 2e^- \rightarrow Fe^{2+}$ (Equation S3)

$Fe^{2+} + 2OH^- \rightarrow Fe(OH)_2\downarrow$ (Equation S4)

In the neutral electrolyte (0.5 M Na_2SO_4, pH = 5.80),

$C(H^+) = 1.58 \times 10^{-6}$ mol L^{-1}

$C(OH^-) = 6.33 \times 10^{-9}$ mol L^{-1}

$K_{sp}(Fe(OH)_2) = 8 \times 10^{-16}$

In the $Fe(OH)_2$, $C(OH^-) = 2C(Fe^{2+})$

$K_{sp}(Fe(OH)_2) = (C(OH^-))^2 \times C(Fe^{2+}) = 4 \times (C(Fe^{2+}))^3$

The $Fe(OH)_2$ would be precipitated with the Fe^{2+} concentration limit of $C(Fe^{2+}) = (K_{sp}(Fe(OH)_2) / 4)^{1/3} = (8 \times 10^{-16} / 4)^{1/3} = 5.8 \times 10^{-6}$ mol L^{-1}.

Under the experimental conditions, the generated current is 0.1 A and the volume of the electrolyte is 100 mL. Hence, the time required for $Fe(OH)_2$ precipitation can be calculated as follows: $t = 2 \times F \times n / i = (2 \times 96485$ C $mol^{-1} \times 5.8 \times 10^{-6}$ mol $L^{-1} \times 0.1$ L) / 0.1 A = 1.12 s, where t is the time required to form $Fe(OH)_2$ precipitate, F is Faraday's constant, n is the molar mass, and i is current.

Supporting Note 5. Electricity consumption and material transformation

With regard to Fig. 4, the video in supporting information, as well as polarization curve in Fig. 3c, $I = 0.1$ A and $U = 1.76$ V are used to evaluate the cost of the hydrogen production system. The electrolyte is a 100 mL neutral aqueous solution (0.5 M Na_2SO_4) containing RhB. The results show that RhB can be recovered completely within 30 min. Therefore, the electricity and materials consumption in this duration can be estimated as follows.

Electricity:

$W_{100} = U \times I \times t = 1.76$ V × 0.1 A × 30 min / 60 min $h^{-1} = 8.80 \times 10^{-5}$ kWh per 100 mL wastewater. To treat 1 T (ton) wastewater, the electricity requirement is calculated approximately as follows: $W_{1\ T} = 10000 \times W_{100} = 0.88$ kWh.

Fe upgrading at the anode:

$CON_{Fe,\ 100} = I \times t / 2 \times F = (0.1\ A \times 30\ min \times 60\ s\ min^{-1}) / (2 \times 96485) = 9.33 \times 10^{-4}$ mol = 52.24 mg per 100 mL wastewater. To treat 1 T wastewater, Fe upgrading is calculated as follows: $CON_{Fe,\ 1\ T} = 10000 \times 52.24$ mg = 522.40 g. The final product of Fe is identified to be Fe_3O_4 nanoparticles. To treat 1 T wastewater, the amount of Fe_3O_4 produced can be calculated as follows: $PRO_{Fe3O4,\ 1\ T} = 10000 \times 9.33 \times 10^{-4}$ mol / 3 × 231.533 g mol^{-1} = 720.07 g. To treat 1 T wastewater, hydrogen production is: $PRO_{H2,\ 1\ T} = 9.33 \times 10^{-4} \times 10000$ = 9.33 mol = 0.23 m^3.

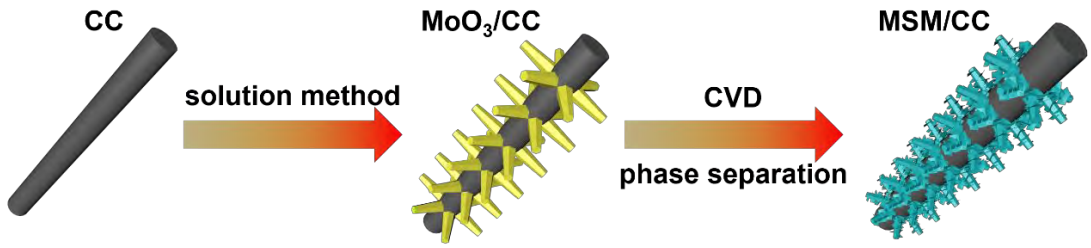

Fig. S1. Schematic depicting the preparation of the core-shell $MoSe_2$ and MoO_2 composite on carbon cloth (MSM/CC).

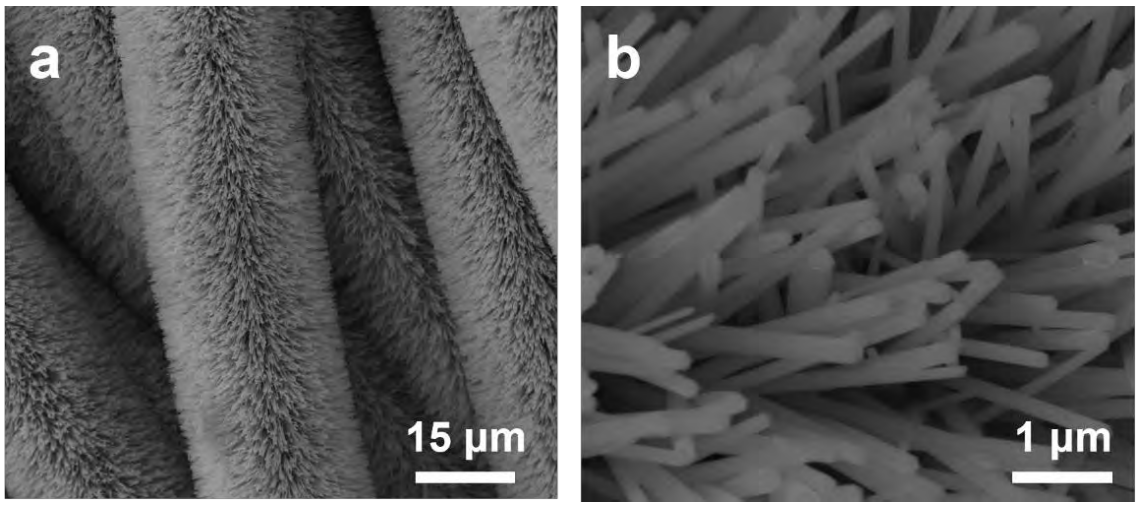

Fig. S2. FE-SEM images of the MoO_3/CC precursor.

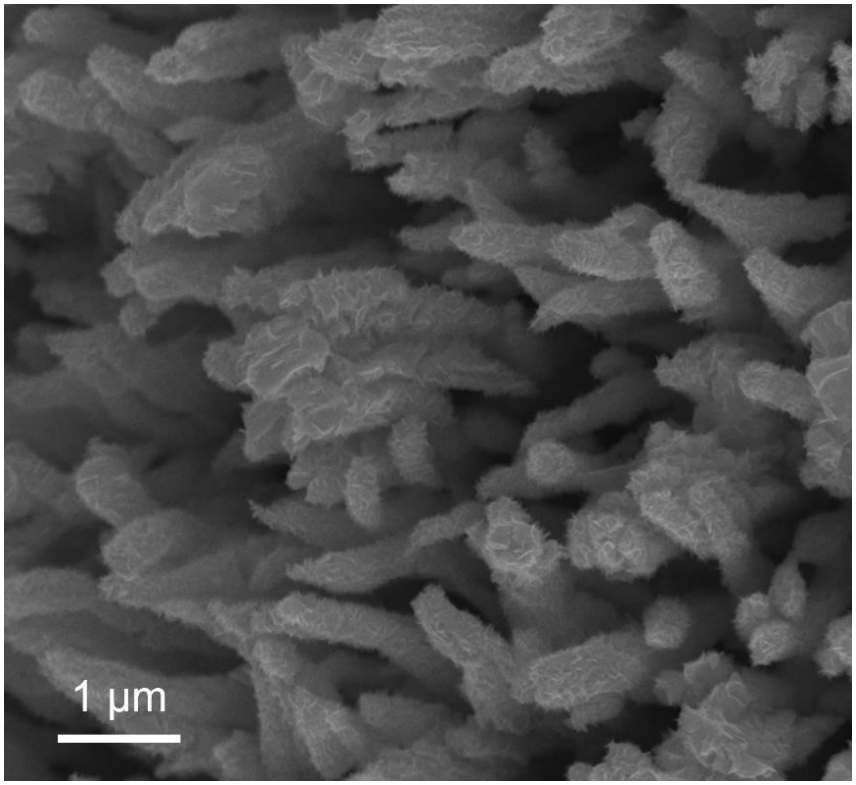

Fig. S3. FE-SEM image of $MoSe_2$/CC.

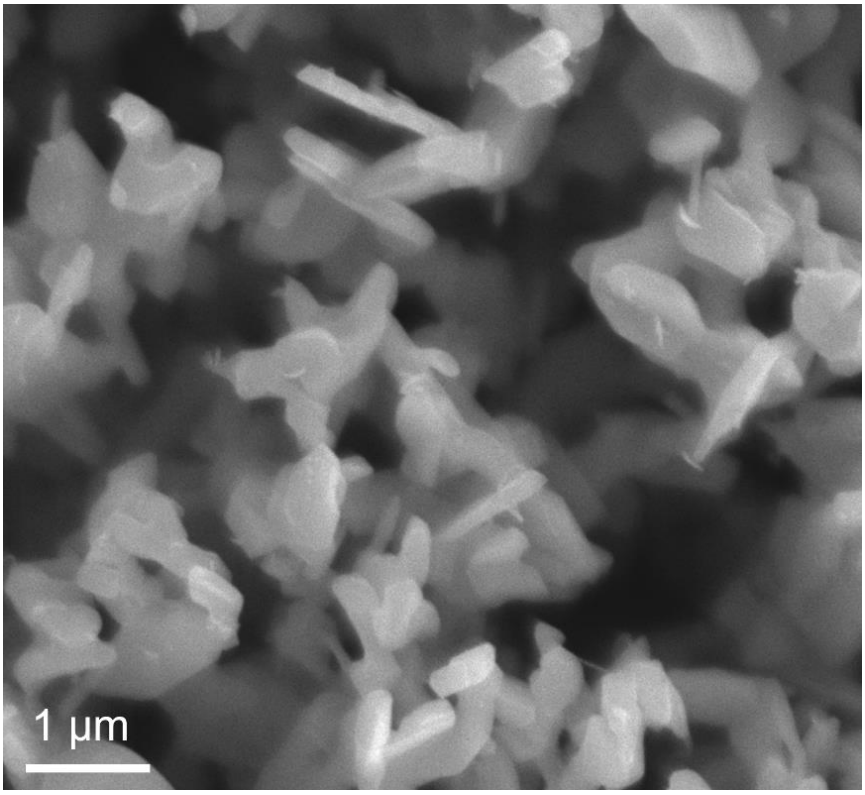

Fig. S4. FE-SEM image of MoO_2/CC.

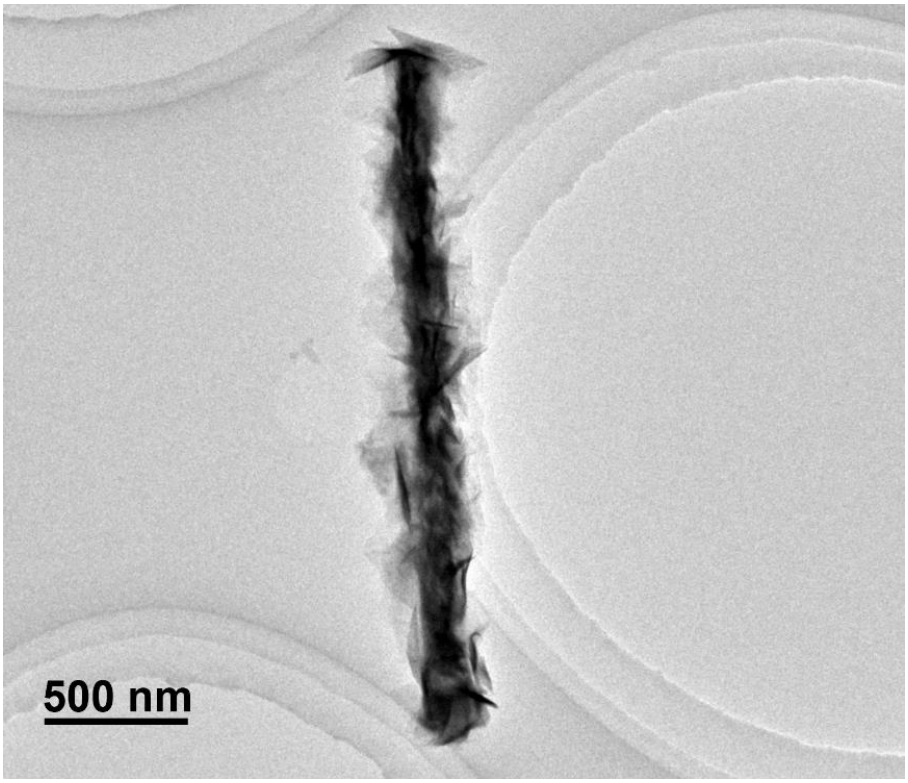

Fig. S5. TEM image of the MSM single nanowire.

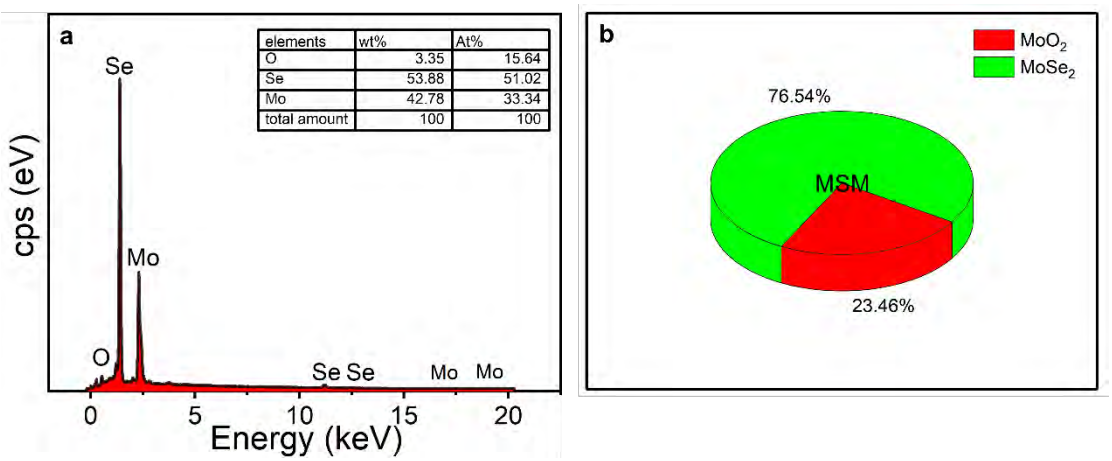

Fig. S6. (a) EDS results and (b) Composition of MSM.

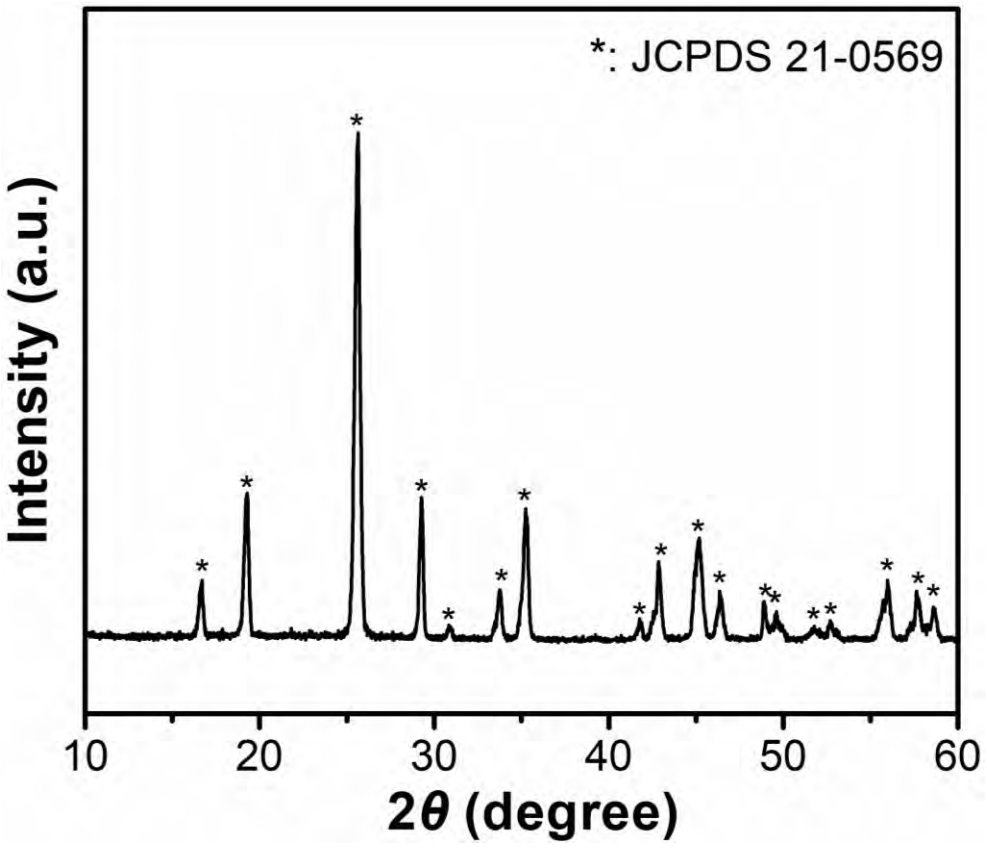

Fig. S7. XRD spectrum of the MoO_3/CC precursor.

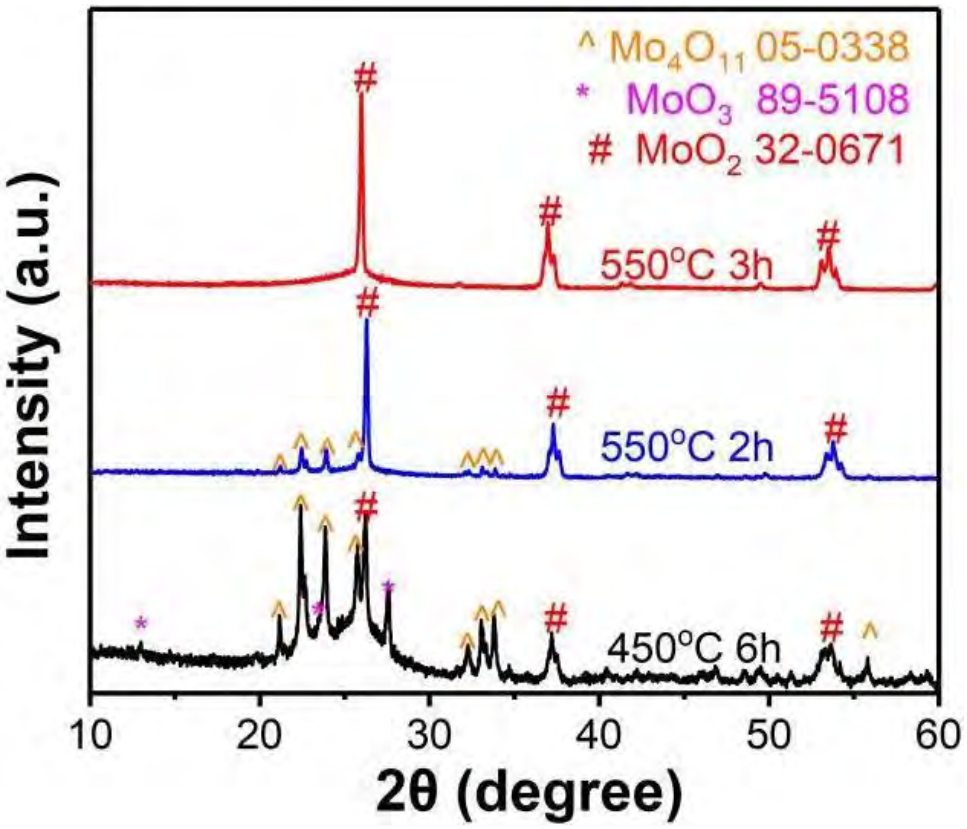

Fig. S8. XRD spectra of MoO_3/CC precursor annealed using different protocols.

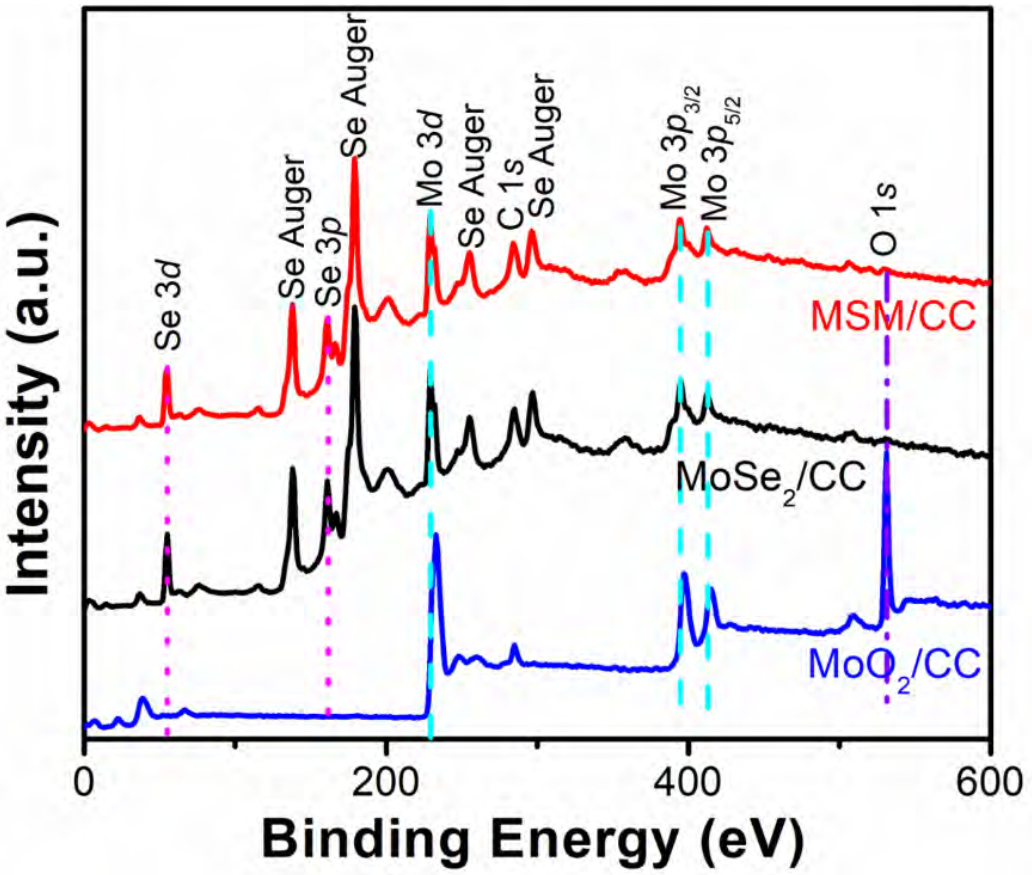

Fig. S9. Survey XPS spectra of the samples.

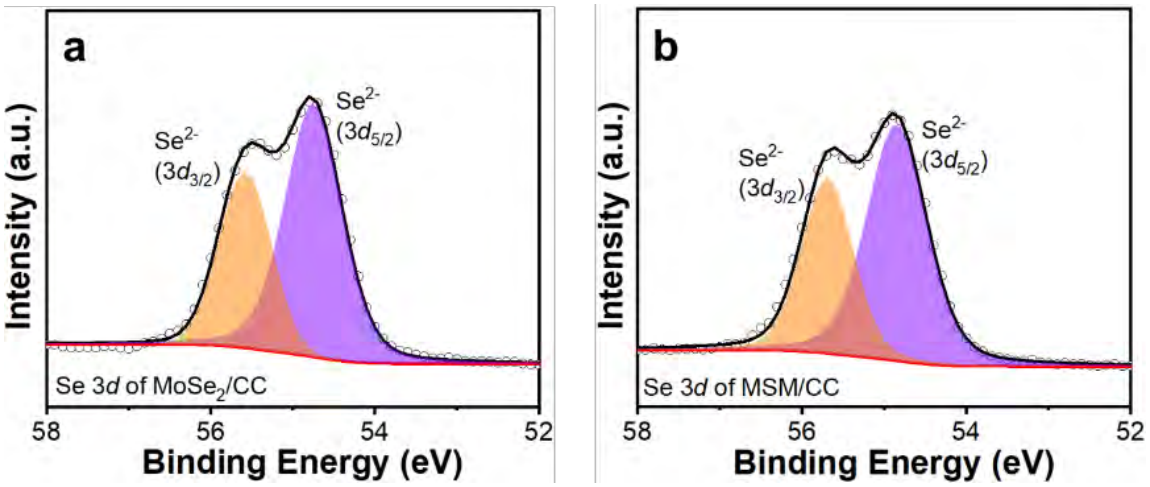

Fig. S10. High-resolution Se 3*d* spectra of (a) $MoSe_2$/CC and (b) MSM/CC.

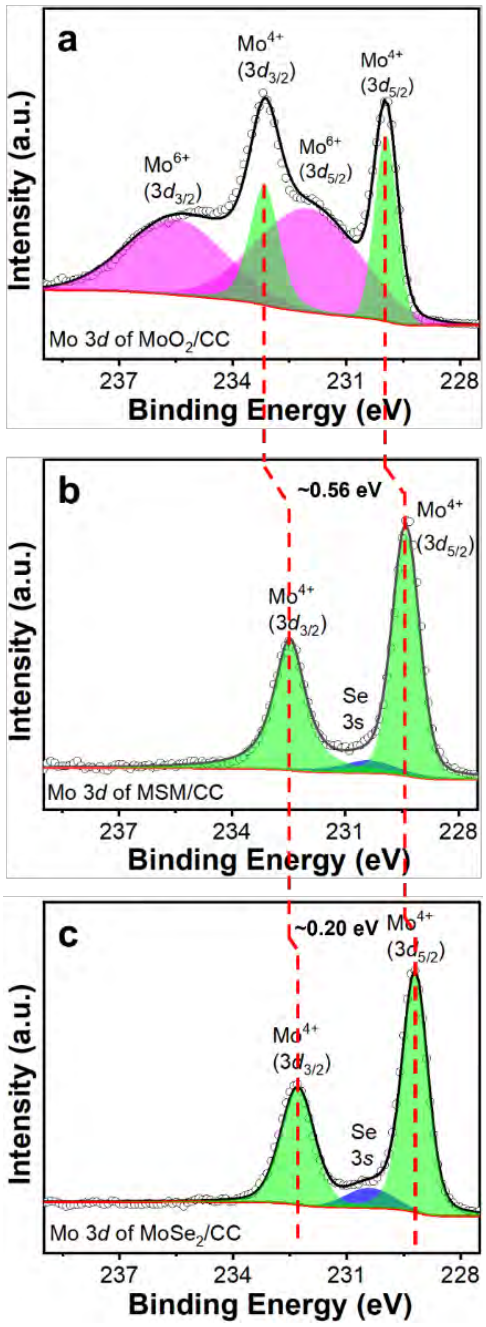

Fig. S11. High-resolution Mo 3*d* spectra of (a) MoO_2/CC, (b) MSM/CC, and (c) $MoSe_2$/CC.

Table S1. Required overpotentials and Tafel slopes for electrocatalysts to generate current densities of 10, 100, and 500 mA cm^{-2}, respectively, in the 1.0 M KOH electrolyte.

Electrocatalysts	η_{10} [mV]	η_{100} [mV]	η_{500} [mV]	Tafel slope [mV dec^{-1}]
MoO_3/CC	363	788	--	385.8
MoO_2/CC	358	459	--	117.6
$MoSe_2$/CC	216	369	--	133.6
MSM/CC	181	293	449	110.4

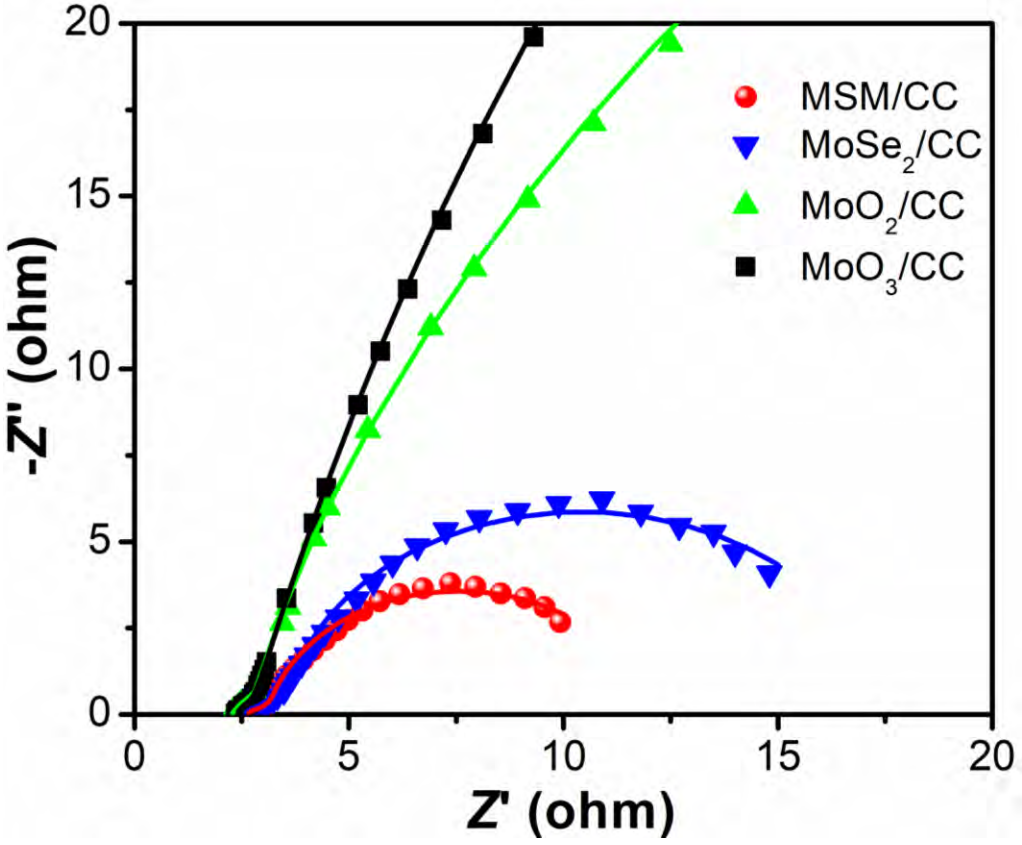

Fig. S12. EIS of the electrocatalysts measured in 1.0 M KOH electrolyte.

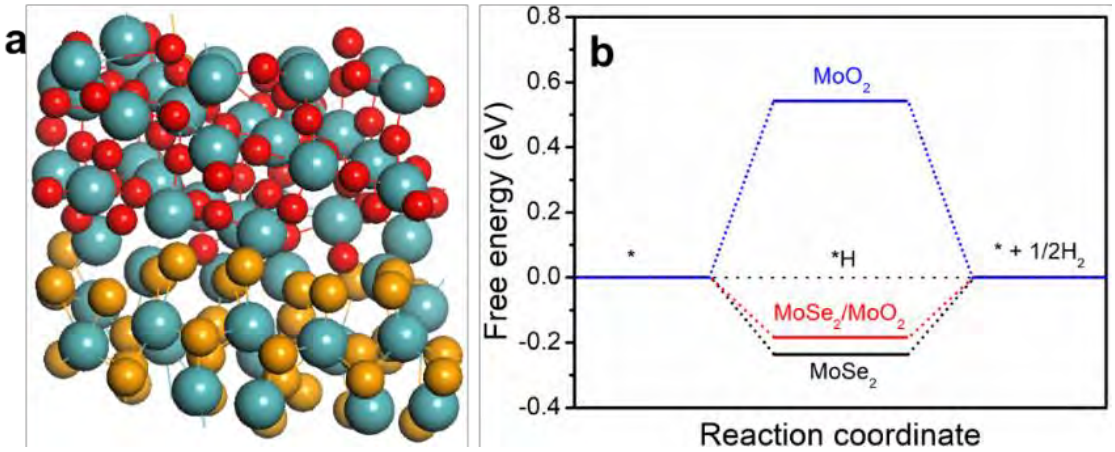

Fig. S13. (a) Simulated model of $MoSe_2/MoO_2$ heterostructure and (b) HER free energy diagrams of the $MoSe_2$, MoO_2, and $MoSe_2/MoO_2$ heterostructure. Blue, brown, and red represent Mo, Se, and O atoms, respectively, and * denotes the clean surface on the electrocatalyst.

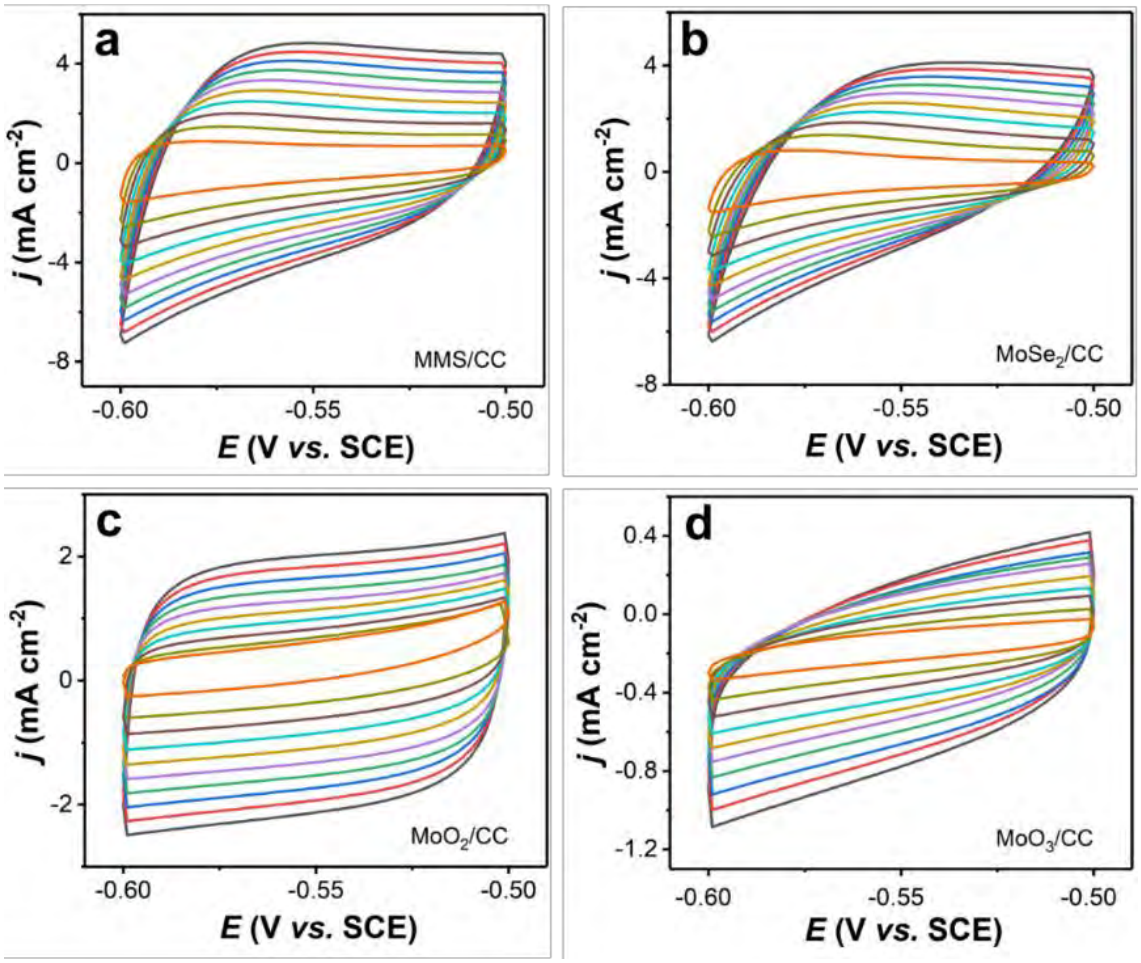

Fig. S14. Cyclic voltammetry curves of the electrocatalysts.

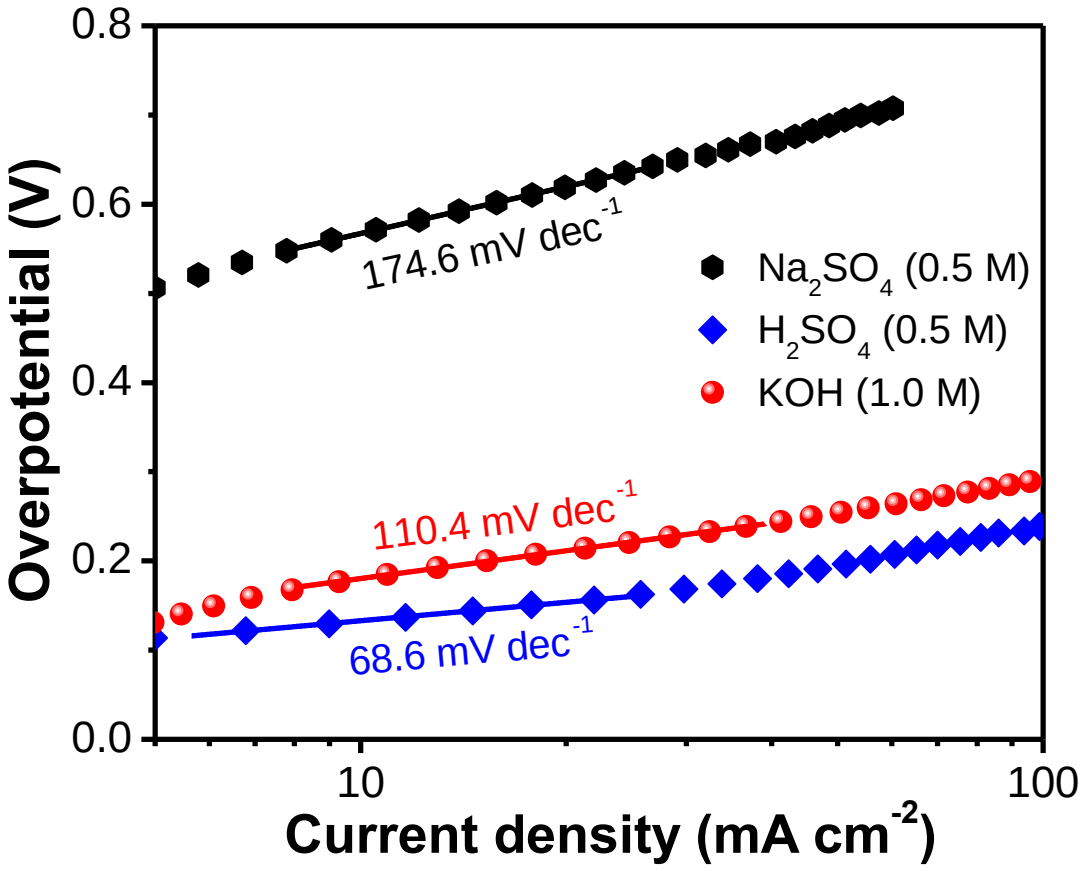

Fig. S15. Tafel slopes of the MSM/CC electrocatalyst in different electrolytes.

Table S2. Required overpotentials and Tafel slopes of the MSM/CC electrocatalyst to generate current densities of 10, 100, and 500 mA cm^{-2} in different electrolytes.

Electrolytes	η_{10} [mV]	η_{100} [mV]	η_{500} [mV]	Tafel slope [mV dec^{-1}]
1.0 M KOH	181	293	449	110.4
0.5 M H_2SO_4	132	240	382	68.6
0.5 M Na_2SO_4	568	--	--	174.6

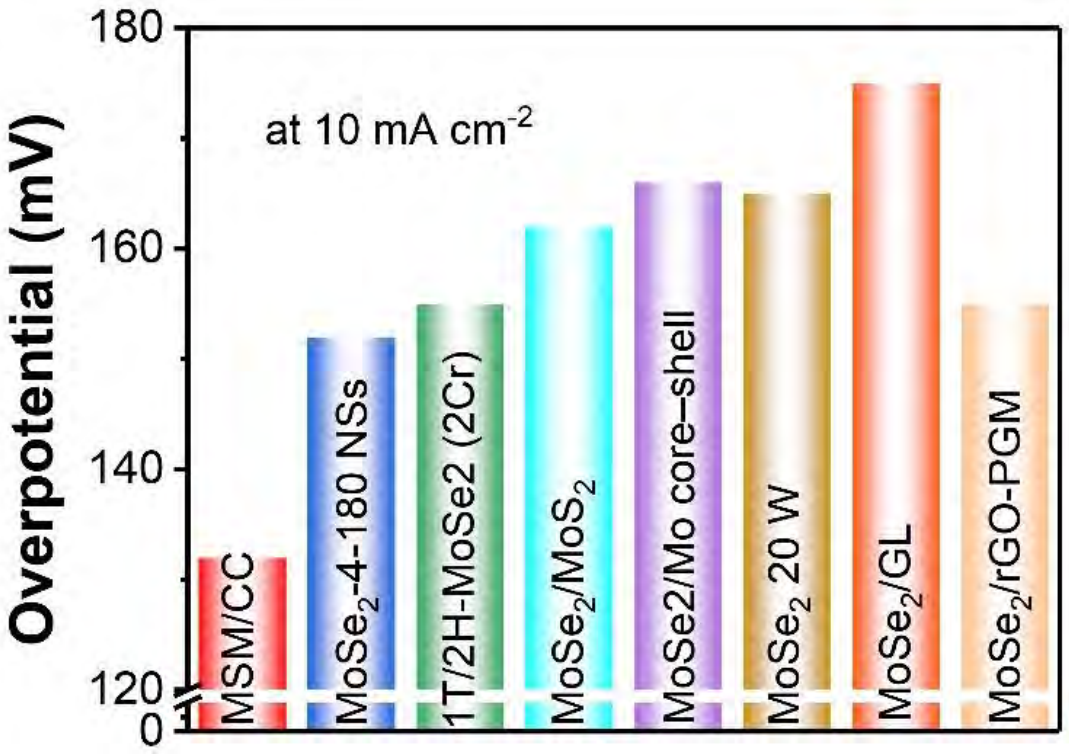

Fig. S16. Comparison of the properties of MSM/CC in this work with those of other reported electrocatalysts in 0.5 M H_2SO_4 including $MoSe_2$-4-180 NSs [7], 1T/2H-$MoSe_2$ (2Cr) [8], $MoSe_2$/MoS_2 [9], $MoSe_2$/Mo core-shell [10], $MoSe_2$ 20 W [11], $MoSe_2$/GL [12], and $MoSe_2$/rGO-PGM [13].

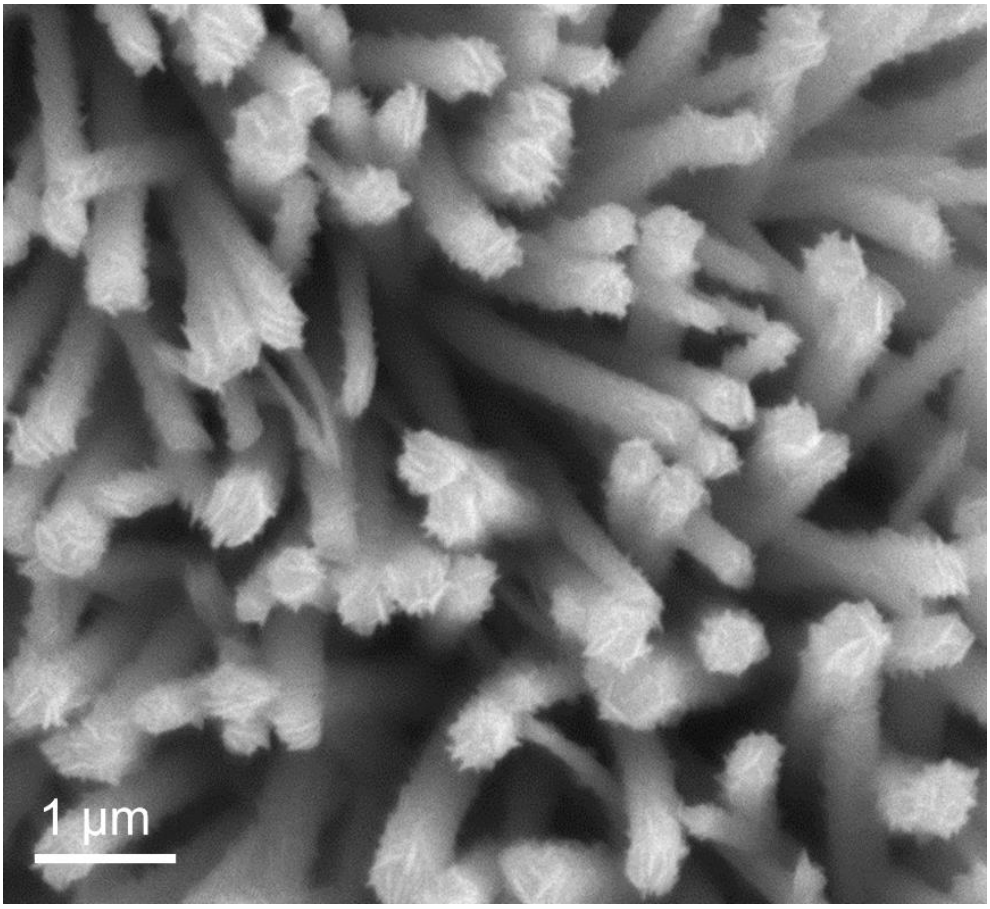

Fig. S17. FE-SEM image of the MSM/CC electrocatalyst after the long-term test.

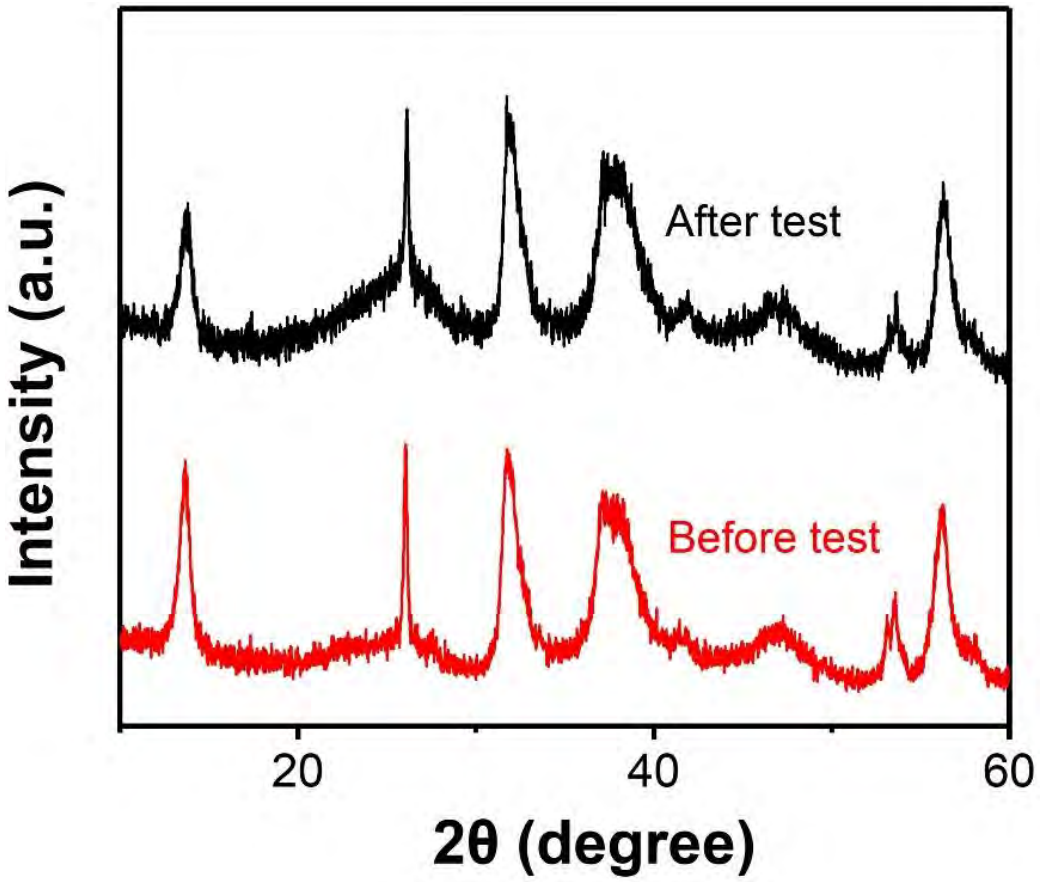

Fig. S18. XRD spectra of the MSM/CC electrocatalyst after the long-term test.

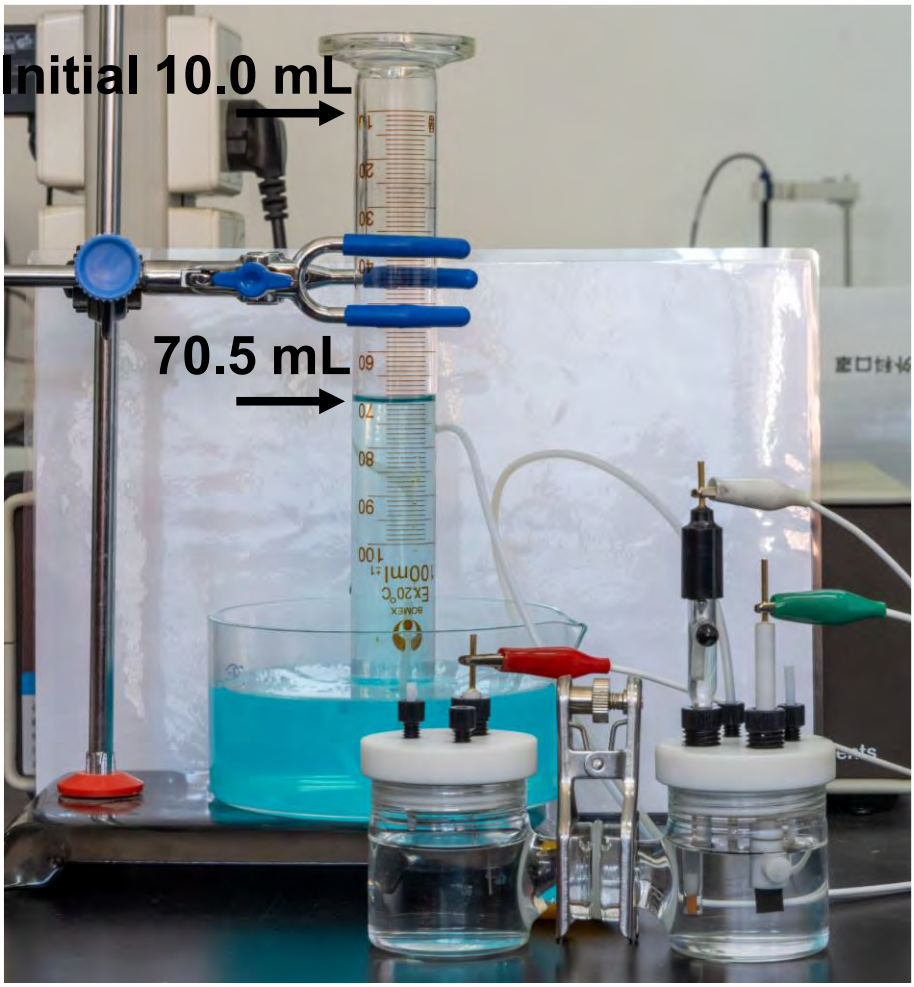

Fig. S19. Photograph of the HER system with the MSM/CC electrocatalyst and H_2 gas generation determined by the water displacement method.

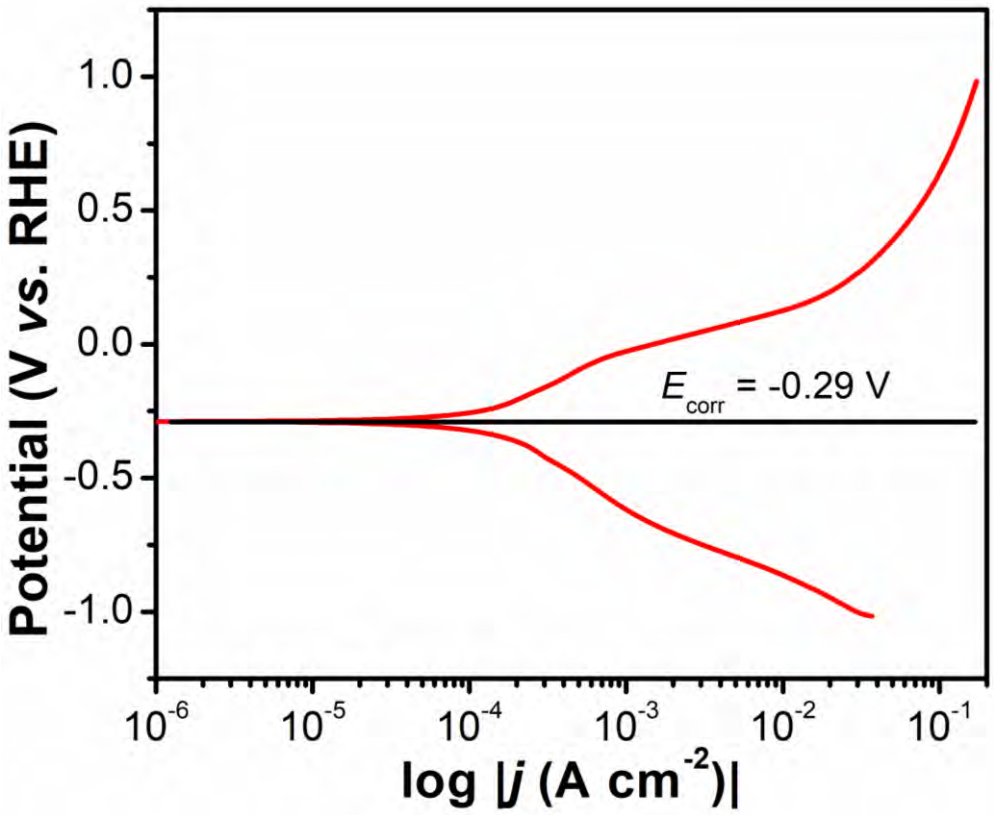

Fig. S20. Tafel plot of the Fe electrode (waste steel rod).

Fig. S21. Photograph of waste steel rods used for construction.

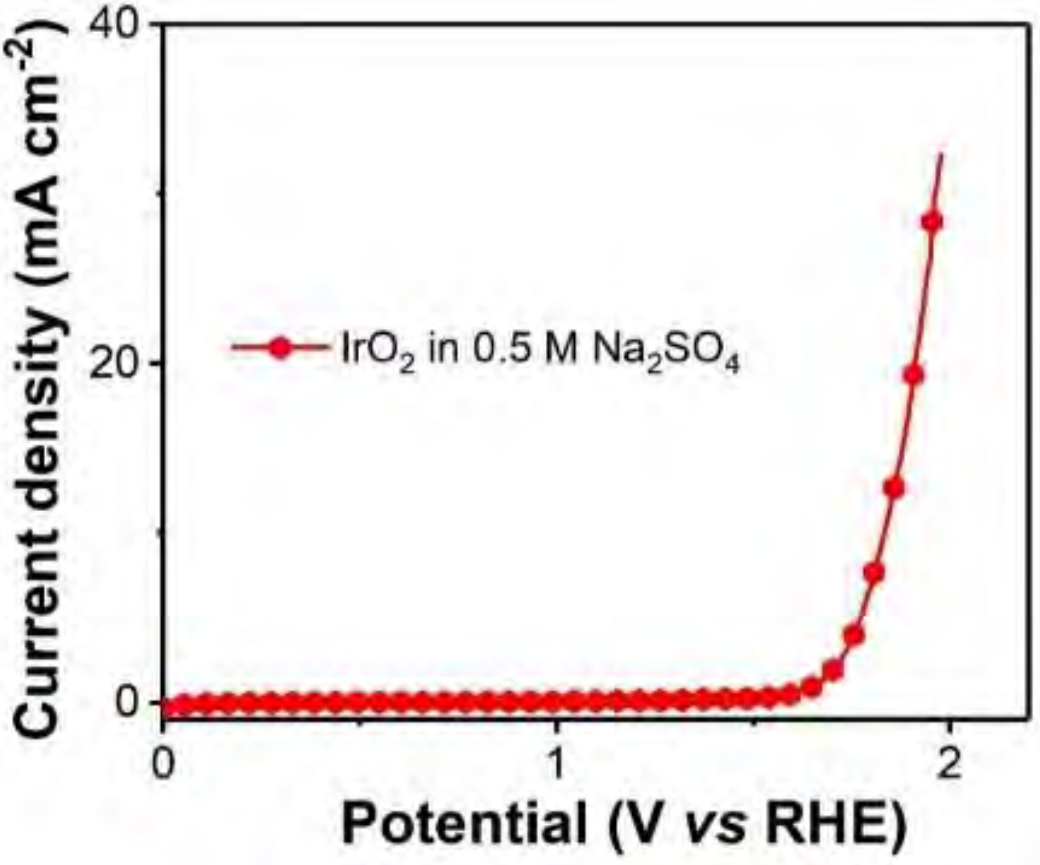

Fig. S22. Polarization curve of commercial IrO_2 in the neutral electrolyte (0.5 M Na_2SO_4).

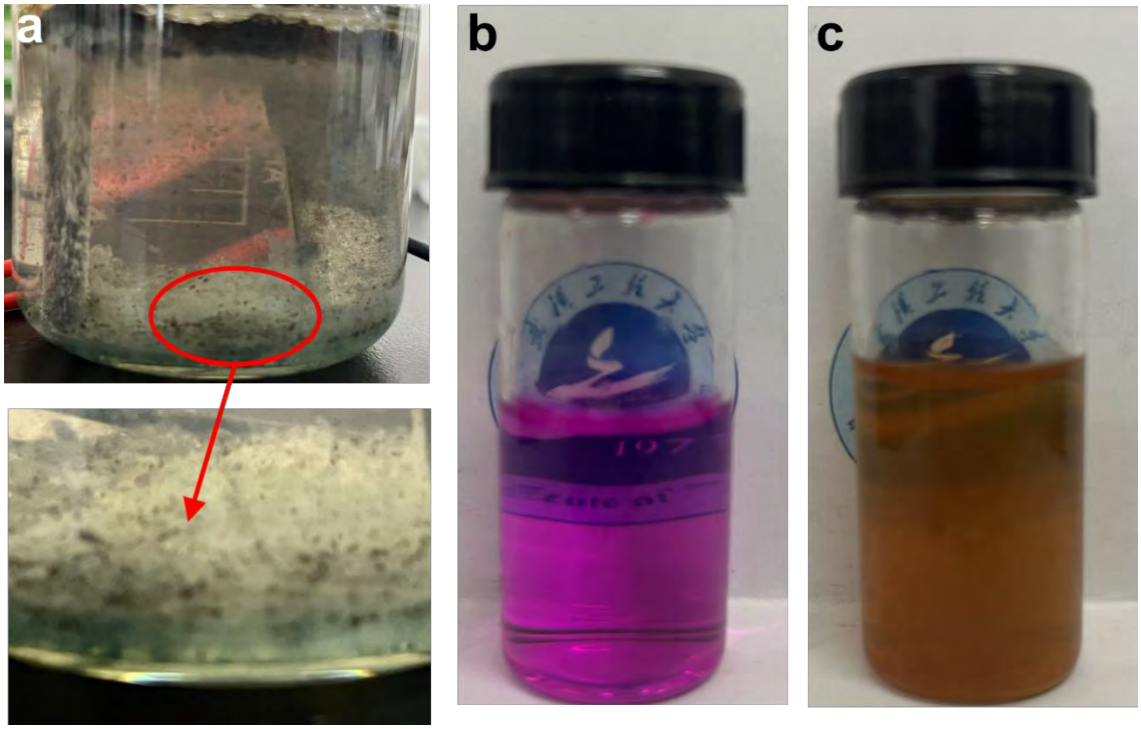

Fig. S23. (a) Photographs of the FUR product and $KMnO_4$ aqueous solution (b) before and (c) after the placement of the final electrolyte for FUR.

Table S3. Comparison of the voltages required by the MSM/CC-Fe couple in a neutral electrolyte with those previously reported for water splitting.

Catalysts	**Electrolytes**	**Couples**	V_{10} [V]	**Ref.**
MSM/CC	0.5 M Na_2SO_4	HER/FOR	0.68	This work
MIL-53(RuNiFe)@NF	1.0 M KOH	OER/HER	1.48	[14]
Se-(NiCo)S_x/OH_x	1.0 M KOH	OER/HER	1.60	[15]
Ru-Ru_2PΦNPC||NPC@RuO_2	0.5 M H_2SO_4	OER/HER	1.50	[16]
3DG-Mix	1.0 M KOH	OER/HER	1.54	[17]
	0.5 M H_2SO_4		1.45	
$RuIrO_x$	1.0 M PBS	OER/HER	1.51	[18]
	1.0 M KOH		1.47	
Co-RuIr||Co-RuIr	0.1 M HClO4	OER/HER	1.52	[19]

Ni_3N-VN/NF||Ni_2P-VP_2/NF	1.0 M KOH	OER/HER	1.51	[20]
porous MoO_2	1.0 M KOH	OER/HER	1.53	[21]
	0.5 M H_2SO_4		1.61	
Mo-Ni-P	1.0 M PBS	OER/HER	1.81	[22]
	1.0 M KOH		1.53	
	0.5 M H_2SO_4		1.75	
PMFCP	1.0 M PBS	OER/HER	1.82	[23]
	1.0 M KOH		1.61	
IrNi NCs	0.5 M H_2SO_4	OER/HER	1.58	[24]
IrNiCu HCSA	0.5 M H_2SO_4	OER/HER	1.53	[25]
1%Cu:α-$Ni(OH)_2$/NF	1 M KOH+0.33 M urea	UOR/HER	1.49	[26]
Ni@C-250	1 M KOH+0.33 M urea	UOR/HER	1.46	[27]
NFO	1 M KOH+0.33 M urea	UOR/HER	1.46	[28]
Ni_2P/CFC	1 M KOH+0.33 M urea	UOR/HER	1.48	[29]

CNTs@Co/CoP	1 M KOH+0.5 M glucose	GOR/HER	1.42	[30]
Ru@Ni-B/NF	1 M KOH+0.1 M glucose	GOR/HER	1.24	[31]
$Ni(OH)_2$/NF	1 M KOH+0.5 M CH_3OH	MOR/HER	1.52	[32]
NiS/NF	1 M KOH+1 M CH_3OH	MOR/HER	1.50	[33]

[a] V_{10} represents the voltage required to generate the current density of 10 mA cm^{-2}.

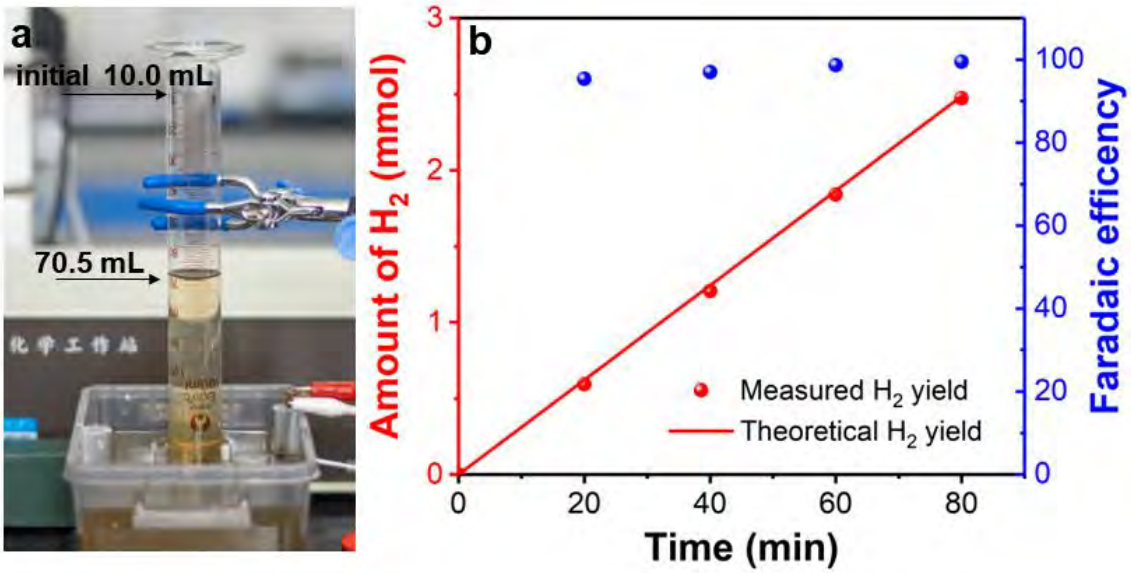

Fig. S24. (a) Photograph of the HER/FUR system with the MSM/CC electrocatalyst and H_2 gas generation determined by the water displacement method; (b) Experimental and theoretical amounts of H_2 produced by the HER/FUR system and Faradaic efficiency at 100 mA.

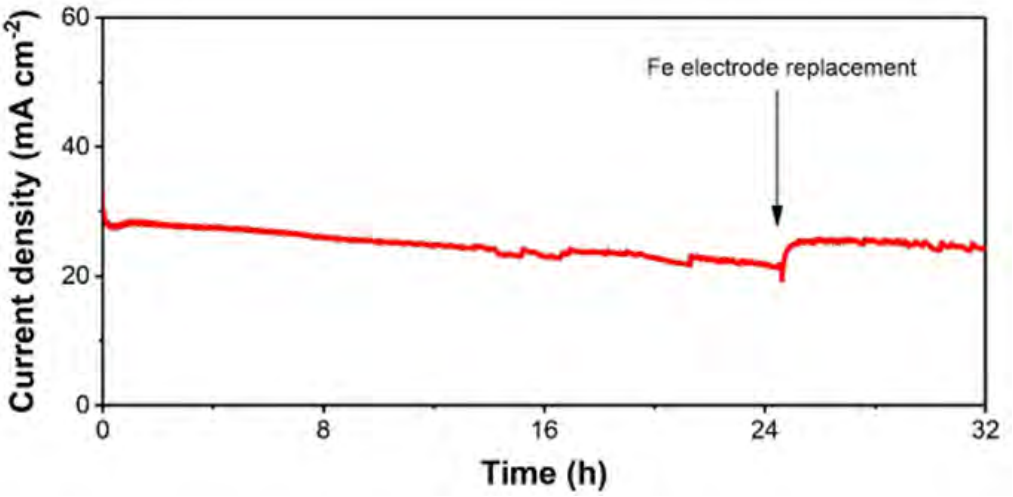

Fig. S25. Stability of HER/FUR system in 0.5 M Na_2SO_4

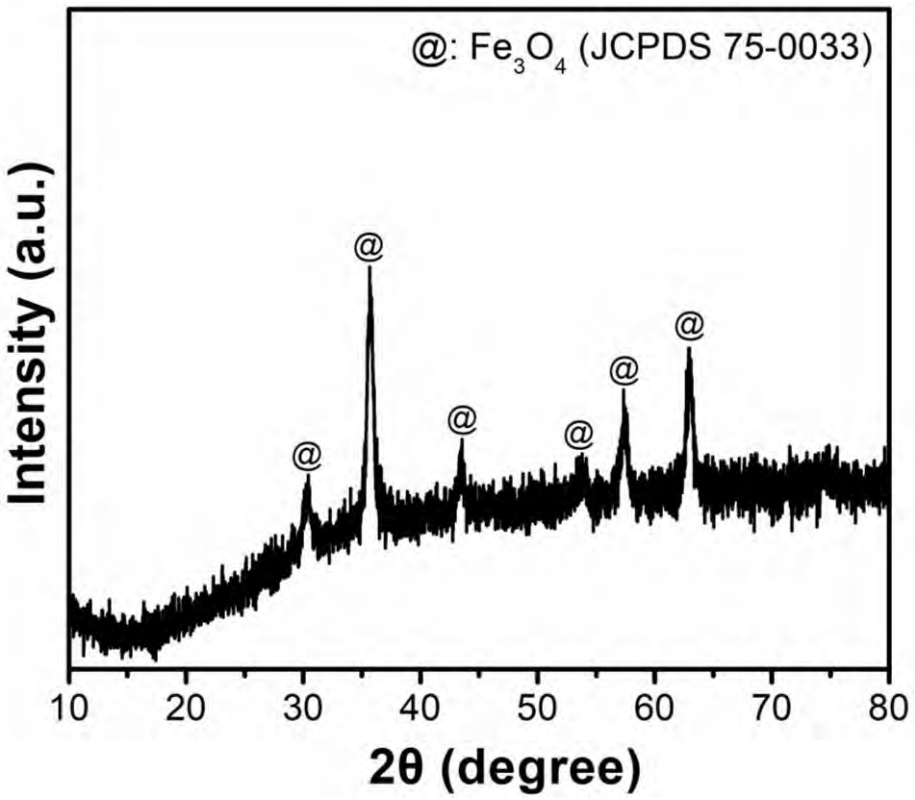

Fig. S26. XRD spectrum of the precipitated floccule in HER/FUR.

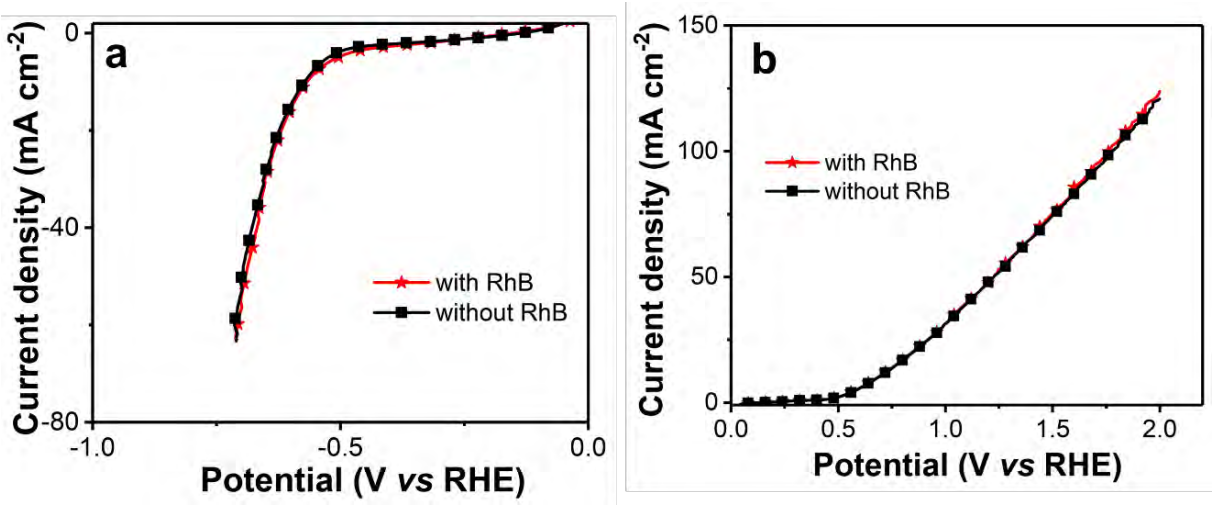

Fig. S27. Polarization curves of (a) HER and (b) FUR with and without RhB in the electrolyte.

Fig. S28. Pictures of the HER/FUR electrolyte in different states.

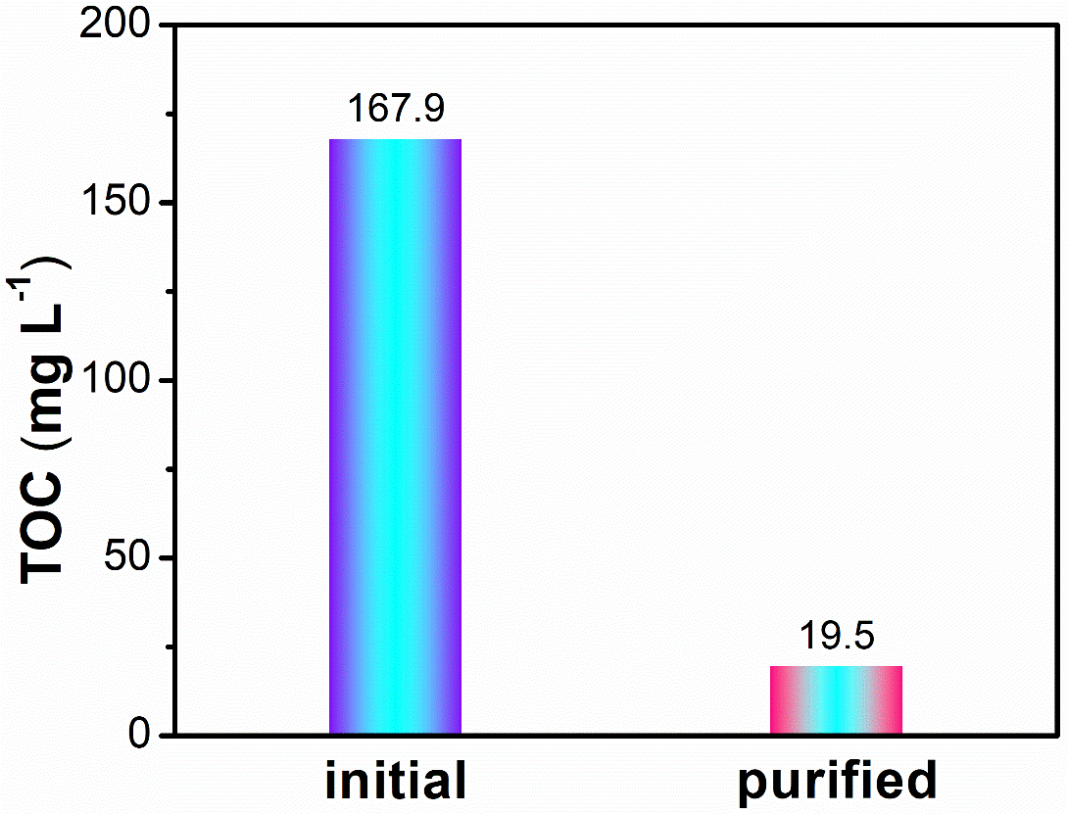

Fig. S29. Total organic carbon (TOC) of the initial and purified electrolyte.

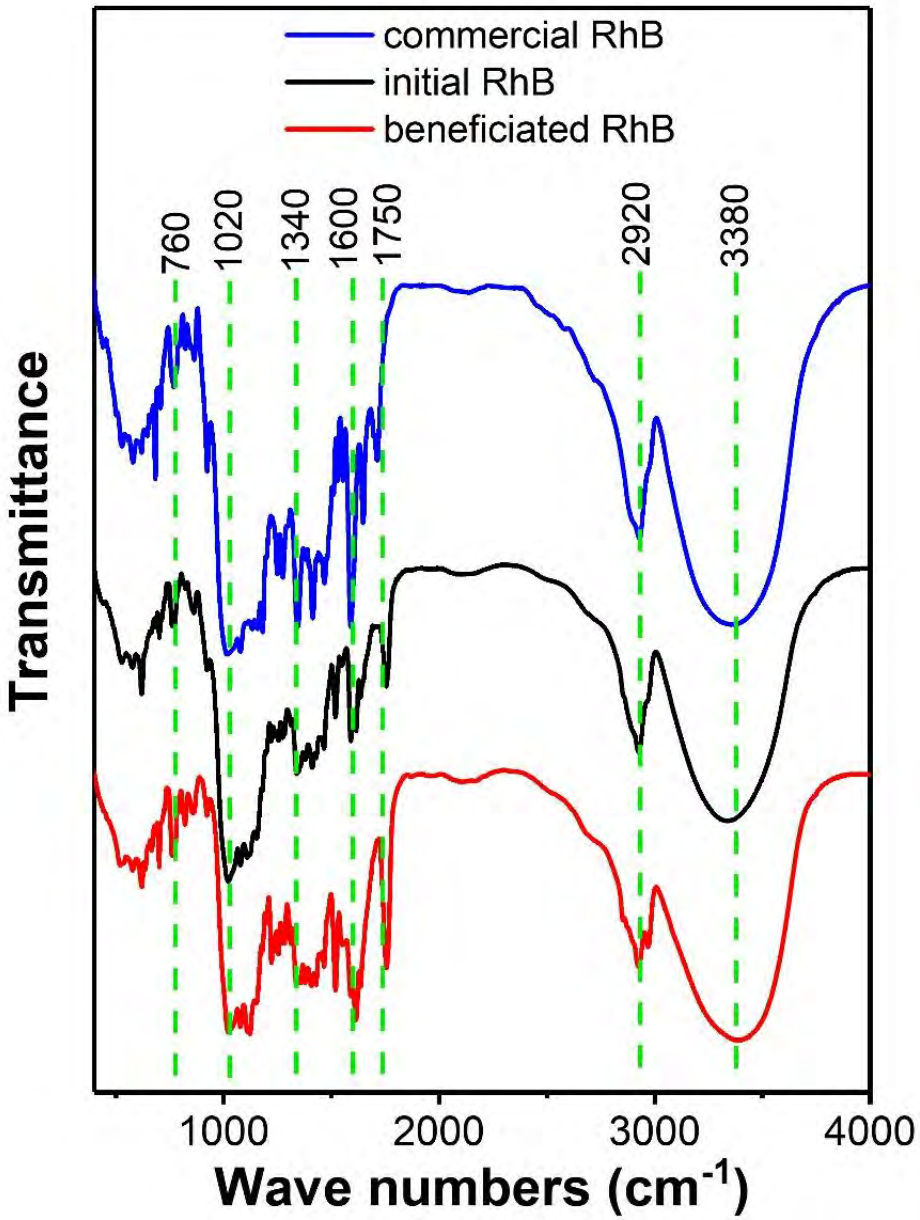

Fig. S30. FTIR spectra of commercial RhB, initial RhB in the electrolyte, and final beneficiated RhB.

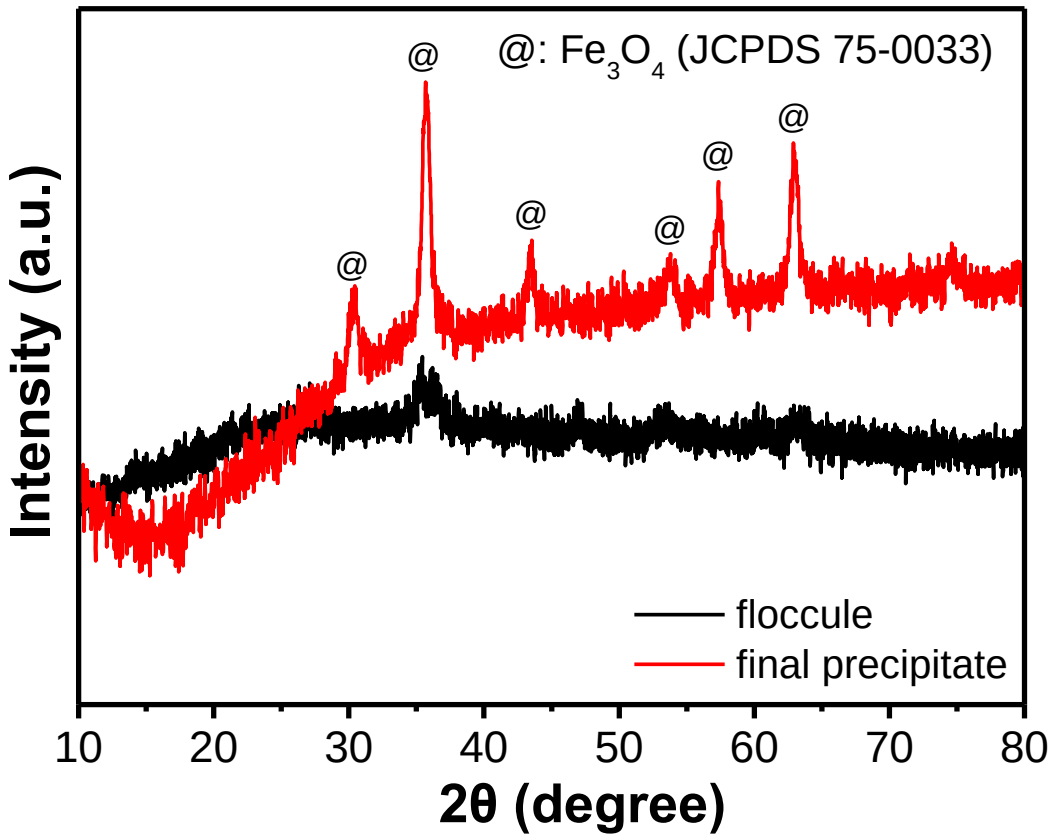

Fig. S31. XRD spectra of the floccule and final precipitate after RhB release with RhB in the initial electrolyte.

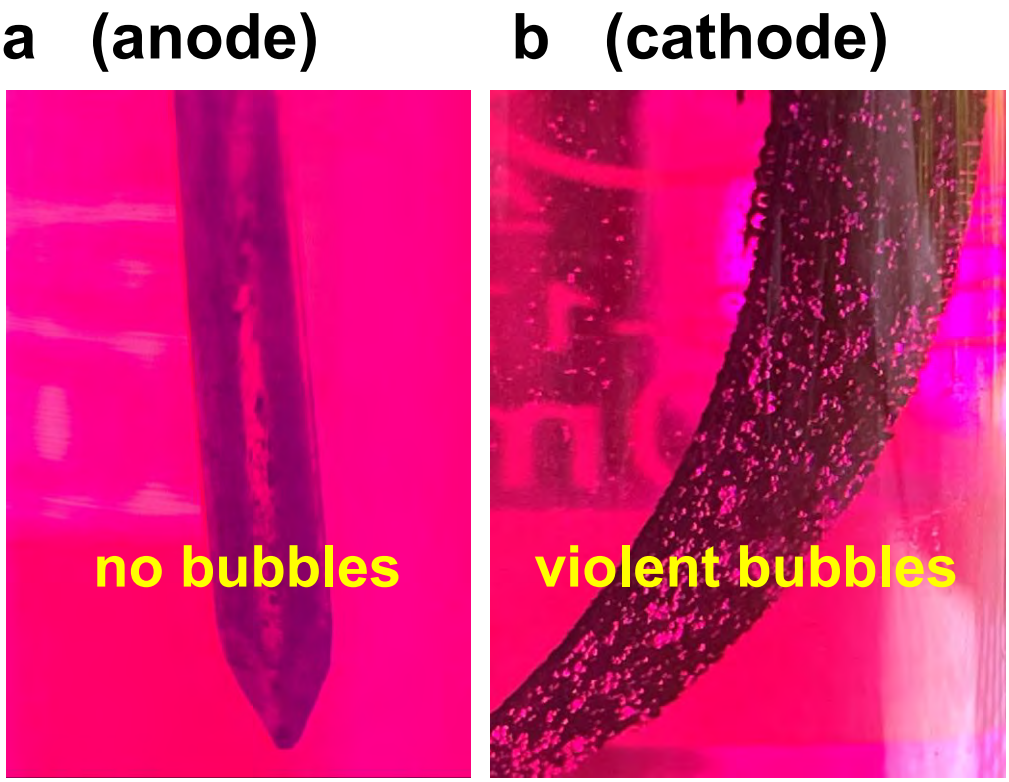

Fig. S32. Photographs of (a) Anode and (b) Cathode in the HER/FUR reaction.

References

[1] B. Delley, J. Chem. Phys., 92 (1990) 508-517.

[2] J.P. Perdew, K. Burke, M. Ernzerhof, Phys. Rev. Lett., 77 (1996) 3865-3868.

[3] S. Grimme, J. Comput. Chem., 25 (2004) 1463-1473.

[4] S. Grimme, J. Comput. Chem., 27 (2006) 1787-1799.

[5] L. Xiong, Z. Sun, X. Zhang, L. Zhao, P. Huang, X. Chen, H. Jin, H. Sun, Y. Lian, Z. Deng, M.H. Rümmerli, W. Yin, D. Zhang, S. Wang, Y. Peng, Nat. Commun., 10 (2019) 3782.

[6] C. Pi, Z. Zhao, X. Zhang, B. Gao, Y. Zheng, P.K. Chu, L. Yang, K. Huo, Chem. Eng. J., 416 (2021) 129130.

[7] Y. Yin, Y. Zhang, T. Gao, T. Yao, X. Zhang, J. Han, X. Wang, Z. Zhang, P. Xu, P. Zhang, Adv. Mater., 29 (2017) 1700311.

[8] A. Mondal, H.R. Inta, V. Bheemireddy, S. Ghosh, V. Mahalingam, ChemNanoMat, 7 (2021) 1063-1071.

[9] S. Li, W. Zang, X. Liu, S.J. Pennycook, Z. Kou, C. Yang, C. Guan, J. Wang, Chem. Eng. J., 359 (2019) 1419-1426.

[10] Y. Qu, H. Medina, S.-W. Wang, Y.-C. Wang, C.-W. Chen, T.-Y. Su, A. Manikandan, K. Wang, Y.-C. Shih, J.-W. Chang, H.-C. Kuo, C.-Y. Lee, S.-Y. Lu, G. Shen, Z.M. Wang, Y.-L. Chueh, Adv. Mater., 28 (2016) 9831-9838.

[11] D. Xiao, D.-L. Bao, X. Liang, Y. Wang, J. Shen, C. Cheng, P.K. Chu, Appl. Catal. B-Environ., 288 (2021) 119983.

[12] D. Xiao, C. Huang, Y. Luo, K. Tang, Q. Ruan, G. Wang, P.K. Chu, ACS Appl. Mater. Interfaces, 12 (2020) 2460-2468.

[13] S. Poorahong, C. Somnin, I. Malam Mahamadou, C. Dubois, S. Chergui, Z. Peng, Y. Su, T. Xuan Tran, C. Thammakhet-Buranachai, A. Mazzah, M. Siaj, ACS Appl. Nano Mater., 5 (2022) 2769-2778.

[14] M. Zhao, H. Li, W. Li, J. Li, L. Yi, W. Hu, C.M. Li, Chem. Eur. J., 26 (2020) 17091-17096.

[15] C. Hu, L. Zhang, Z.-J. Zhao, A. Li, X. Chang, J. Gong, Adv. Mater., 30 (2018) 1705538.

[16] J. Yu, G. Li, H. Liu, L. Zhao, A. Wang, Z. Liu, H. Li, H. Liu, Y. Hu, W. Zhou, Adv. Funct. Mater., 29 (2019) 1901154.

[17] S. Riyajuddin, S.K. Tarik Aziz, S. Kumar, G.D. Nessim, K. Ghosh, ChemCatChem, 12 (2020) 1394-1402.

[18] Z. Zhuang, Y. Wang, C.-Q. Xu, S. Liu, C. Chen, Q. Peng, Z. Zhuang, H. Xiao, Y. Pan, S. Lu, Nat. Commun., 10 (2019) 1-10.

[19] J. Shan, T. Ling, K. Davey, Y. Zheng, S.Z. Qiao, Adv. Mater., 31 (2019) 1900510.

[20] H. Yan, Y. Xie, A. Wu, Z. Cai, L. Wang, C. Tian, X. Zhang, H. Fu, Adv. Mater., 31 (2019) 1901174.

[21] Y. Jin, H. Wang, J. Li, X. Yue, Y. Han, P.K. Shen, Y. Cui, Adv. Mater., 28 (2016) 3785-3790.

[22] C. Lai, X. Liu, Y. Wang, C. Cao, Y. Yin, H. Yang, X. Qi, S. Zhong, X. Hou, T. Liang, Electrochim. Acta, 330 (2020) 135294.

[23] H. Liu, X. Peng, X. Liu, G. Qi, J. Luo, ChemSusChem, 12 (2019) 1334-1341.

[24] Y. Pi, Q. Shao, P. Wang, J. Guo, X. Huang, Adv. Funct. Mater., 27 (2017) 1700886.

[25] J. Zhang, Z. Chen, C. Liu, J. Zhao, S. Liu, D. Rao, A. Nie, Y. Chen, Y. Deng, W. Hu, Sci. China Mater., 63 (2020) 249-257.

[26] J. Xie, L. Gao, S. Cao, W. Liu, F. Lei, P. Hao, X. Xia, B. Tang, J. Mater. Chem. A, 7 (2019) 13577-13584.

[27] J. Wang, Z. Zhao, C. Shen, H. Liu, X. Pang, M. Gao, J. Mu, F. Cao, G. Li, Catal. Sci. Technol., 11 (2021) 2480-2490.

[28] F. Wu, G. Ou, J. Yang, H. Li, Y. Gao, F. Chen, Y. Wang, Y. Shi, Chem. Commun., 55 (2019) 6555-6558.

[29] X. Zhang, Y. Liu, Q. Xiong, G. Liu, C. Zhao, G. Wang, Y. Zhang, H. Zhang, H. Zhao, Electrochim. Acta, 254 (2017) 44-49.

[30] Y. Zhang, Y. Qiu, Z. Ma, Y. Wang, Y. Zhang, Y. Ying, Y. Jiang, Y. Zhu, S. Liu, J. Mater. Chem. A, 9 (2021) 10893-10908.

[31] H. Liu, R. Zhang, L. Chen, L. Wang, Y. Guo, Y. Yang, Adv. Sustain. Syst., 5 (2021) 2000184.

[32] J. Hao, J. Liu, D. Wu, M. Chen, Y. Liang, Q. Wang, L. Wang, X.-Z. Fu, J.-L. Luo, Appl. Catal. B-Environ., 281 (2021) 119510.

[33] Z. Pi, H. Zhong, IOP Conf. Ser.: Earth Environ. Sci., 651 (2021) 042062.